

Monte Carlo Simulations of Nematic Liquid Crystal Defects and Mixtures

by Nathaniel Tarshish

Advisor: Prof. Robert Pelcovits

A thesis submitted in partial fulfillment of the requirements for the Degree of
Bachelor of Science in the Department of Physics at Brown University

May 2016

Acknowledgments

I am thankful for the generosity and guidance of my advisor, Professor Pelcovits, who gave me the freedom and tools to explore my interests and always patiently assisted me whenever I asked for help. I would like to thank my friends Alex Varga, Dan Meyers, and especially Alex Ashery, for their programming advice. My surrogate parents in Providence, Dan Meyers and Alexia Ramirez, graciously provided home-cooked meals and a couch that I very much appreciated over this past year.

Finally, I am deeply grateful to my family and Hannah Kerman for being a source of unflagging support, love, and strength.

Contents

1	Introduction	1
1.1	Overview	1
1.2	The Liquid Crystal Phase	1
1.3	The Order Parameter	3
2	Computer Simulation of Liquid Crystals	7
2.1	The Model	7
2.2	Monte Carlo Methods	8
2.2.1	Metropolis algorithm	11
2.2.2	Liquid Crystal Metropolis Implementation	12
3	Defect Structures	17
3.1	Topology of Defects	17
3.2	Defect Detection	22
3.3	Experimental Defect Induction Techniques	23
3.4	Defect Induction via Boundary Conditions	24
3.4.1	Wedge Disclination Loops	24
3.4.2	Generalizing WDL Boundary Conditions	26
3.4.3	Threading Backer Lines Through Planar Curves	27
4	Multispecies Models	33
4.1	Multispecies Lebwohl-Lasher Model	33
4.2	Multispecies Generalization of the Lebwohl-Lasher Model	34
4.3	Exchange Moves	35
4.4	Interspecies Mixing Correlation Functions	36
4.5	Preliminary Results	38
4.6	Future Investigations	40
Bibliography		41

CHAPTER 1

Introduction

1.1 Overview

In this research, we employ Monte Carlo simulations of nematic liquid crystals to investigate topological defect structures and propose a model capable of simulating multi-species mixing phenomena. In this chapter, we present a brief introduction to the physics, varieties, and applications of liquid crystals. We also present the mathematical tools used to characterize the degree of ordering in liquid molecules, namely the tensor and scalar order parameters. In Chapter 2, we introduce the Lebwohl-Lasher lattice model of a nematic liquid crystal and present the Monte Carlo Metropolis algorithm employed to approximate statistical properties of the liquid crystal. In Chapter 3, we detail the topology of defects in a nematic liquid crystal and the boundary conditions discovered in this research to produce novel defect structures. In Chapter 4, we explain our efforts to simulate the mixing of liquid crystal molecules of different species.

1.2 The Liquid Crystal Phase

In a liquid, molecules enjoy high degrees of rotational and translational freedom. The attractive forces between the liquid molecules maintain uniform density, but individual molecules execute random walks with abrupt changes in direction and orientation. This behavior is in stark contrast with the movement of molecules found in a solid. Strong intermolecular forces lock molecules in a solid into a rigid crystalline structure, fixing the average location and direction that each molecule points in. This rigid structure leaves the solid molecules with little translational or orientational freedom. The properties of liquid crystals straddle the boundary between the solid and liquid phases of matter. Liquid crystal molecules possess a high degree of translational freedom, but alignment forces constrain their orientations to fit into patterns. Depending on the specifics of the liquid crystal, these alignment forces could be due to electrostatic forces, Van der Waals interactions, or geometrical considerations [1].

Translational freedom allows liquid crystals to flow like a fluid, but the orientational order present in the liquid crystal can lead to anisotropic optical, electrical, and structural properties that are typically exhibited by solids. A classic example of such an anisotropic property is the birefringence exhibited by liquid crystals: the transmission of light through the liquid crystal depends on the polarization and direction of propagation of the incoming light. The orientational order within a liquid crystal is also often highly sensitive to external forces such as electric or magnetic fields. Display technologies harness this electrical sensitivity and birefringence to control the emission of light by the liquid crystal pixel. [2]

In a standard LCD pixel, liquid crystal molecules are sandwiched between a pair of crossed polarizers [3]. Without the application of external electric fields, the arrangement of the liquid crystal molecules

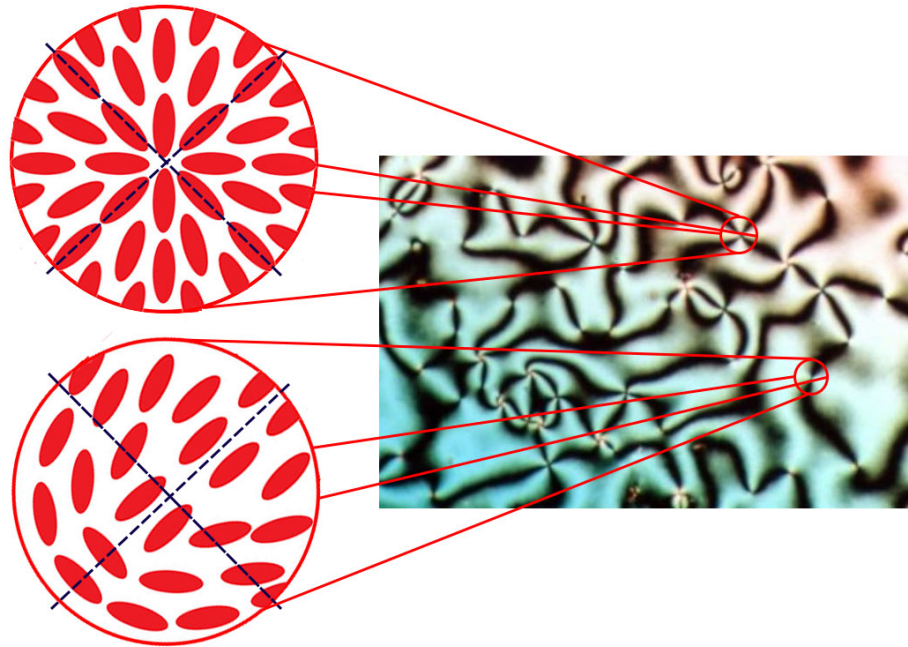


Figure 1.1: a nematic sample between crossed polarizers exhibiting a schlieren texture. Dark regions indicate where the molecules are aligned or orthogonal to the polarization axis of the first polarizer. Closeups are shown for a 360° point defect and a 180° point defect with the polarization axes indicated by dashed cross-hairs.

enforced by the boundary conditions does not alter the polarization of incoming light. As a result, all the light is blocked by the second polarizer. When an electric field is applied, the orientational pattern shifts and the interaction of the light with the liquid crystal rotates the light's polarization axis. By varying the strength of the electric field, the amount of light that passes through the second polarizer may be adjusted. Thus, the transmission of light through the liquid crystal cell can be modulated using an electric field.

Figure 1.1 displays a nematic liquid crystal sample that is suspended between two crossed-polarizers. The pattern of dark lines coursing through the liquid crystal is known as a Schlieren texture. Dark regions indicate that the light was blocked by the second polarizer. At these locations, the polarization axis of the incident light was unrotated after interacting with the liquid crystal, implying that the molecular axes of such molecules must be parallel or orthogonal to the axis of the first polarizer. The dark lines coursing through the sample are known as defect disclination lines. The points at which four (two) dark lines intersect are known as 2π (π) point defects. An extensive discussion of these defects is presented Chapter 3.

Aside from their usage in displays, liquid crystals can be found in a host of other technologies and biological systems including protein and virus structures, detergents, and even spider silk [2, 4]. Structures formed by lipids such as the phospholipid bilayer of the cell wall or micelles found in surfactants are well described by the liquid crystal phase. The amphiphilic structure of the lipid molecules gives rise to alignment forces that orient the hydrophilic heads far from the oleophilic tails. In the case of the cell wall, these forces produce the familiar bilayer structure in which the tails of lipids all orient towards the middle of the bilayer. The bilayer demonstrates liquid crystalline properties because the orientation of the lipids remains fixed, but the molecules are free to translationally roam within their monolayer.

In this research, we focus on nematics, a class of liquid crystals comprised of elongated, rod-like molecules. In particular, our research concerns nematics that are uniaxial (i.e., symmetrical about a long

axis like an ellipsoid or rod). Liquid crystals of this type are used in the LCD pixels described earlier in this section. At absolute zero, long-range alignment forces orient the molecules to uniformly point in one direction. At higher temperatures, thermal excitations reduce the degree of orientational ordering and vary the alignments of the molecules. In the following section, we describe the mathematical treatment of the amount of orientational order present in a nematic liquid crystal.

1.3 The Order Parameter

To describe the orientation of nematic molecule, we introduce a unit vector, \vec{v} , that points along the molecule's long axis. Given a sample of such molecules, we describe how the \vec{v} 's corresponding to the different molecules are distributed over the sphere using a distribution function $\phi(\vec{v})$ [3]. Due to the inversion symmetry of the ellipsoidal molecules, the distribution function has the property that $\phi(\vec{v}) = \phi(-\vec{v})$. Let us also introduce the director, \vec{n} , which gives the average orientation of the molecules in the sample [1]. To solve for \vec{n} we cannot simply compute the expected value of the distribution of vectors:

$$\langle \vec{v} \rangle = \int \vec{v} \phi(\vec{v}) d\vec{v} = 0 \quad (1.1)$$

The integral is zero due to the fact that $\vec{v}\phi(\vec{v})$ is an odd function being integrated over a symmetric domain (surface of the unit sphere). To find the director, we have to consider higher moments of the distribution given by $\langle v_i v_j \rangle$ [5].

To gain insight into the properties of this tensor, let's examine its form for the isotropic and aligned phase. In the isotropic case, the molecular orientations are uniformly distributed over a sphere. By symmetry, it follows that $\langle v_x^2 \rangle = \langle v_y^2 \rangle = \langle v_z^2 \rangle$. For $i \neq j$, we find that $\langle v_i v_j \rangle = 0$ due to integration of an odd function over the symmetric domain. Therefore, we have that $\langle v_i v_j \rangle$ is proportional to δ_{ij} . The constant of proportionality is found by noting that

$$\text{Tr}(\langle v_i v_j \rangle) = \langle v_x^2 \rangle + \langle v_y^2 \rangle + \langle v_z^2 \rangle = \langle v_x^2 + v_y^2 + v_z^2 \rangle = 1 \quad (1.2)$$

From this we conclude that $\langle v_i v_j \rangle = 1/3\delta_{ij}$ for the isotropic distribution.

Given the uniformly ordered case, all the molecules point along the director so that $\langle v_i v_j \rangle = \langle n_i n_j \rangle = n_i n_j$. To describe the orientational order for the general case, we compute the tensor order parameter:

$$Q_{ij} = \left\langle v_i v_j - \frac{1}{3}\delta_{ij} \right\rangle \quad (1.3)$$

First, we note that \mathbf{Q} has trace zero:

$$\text{Tr}(\mathbf{Q}) = \text{Tr}(\langle v_i v_j \rangle) - 1 = \langle v_x^2 \rangle + \langle v_y^2 \rangle + \langle v_z^2 \rangle - 1 = \langle v_x^2 + v_y^2 + v_z^2 \rangle - 1 = 0. \quad (1.4)$$

since \vec{v} is a unit vector. Exploiting the symmetries of the tensor allows us to further simplify its form [5]. Because \mathbf{Q} is a symmetric tensor, given a suitable coordinate system, it can be diagonalized such that

$$\mathbf{Q} = \begin{pmatrix} Q^{(1)} & 0 & 0 \\ 0 & Q^{(2)} & 0 \\ 0 & 0 & Q^{(2)} \end{pmatrix} \quad (1.5)$$

The axes of the coordinate system that diagonalizes the matrix form the eigenbasis: $\mathbf{e}^{(1)}, \mathbf{e}^{(2)}, \mathbf{e}^{(3)}$.

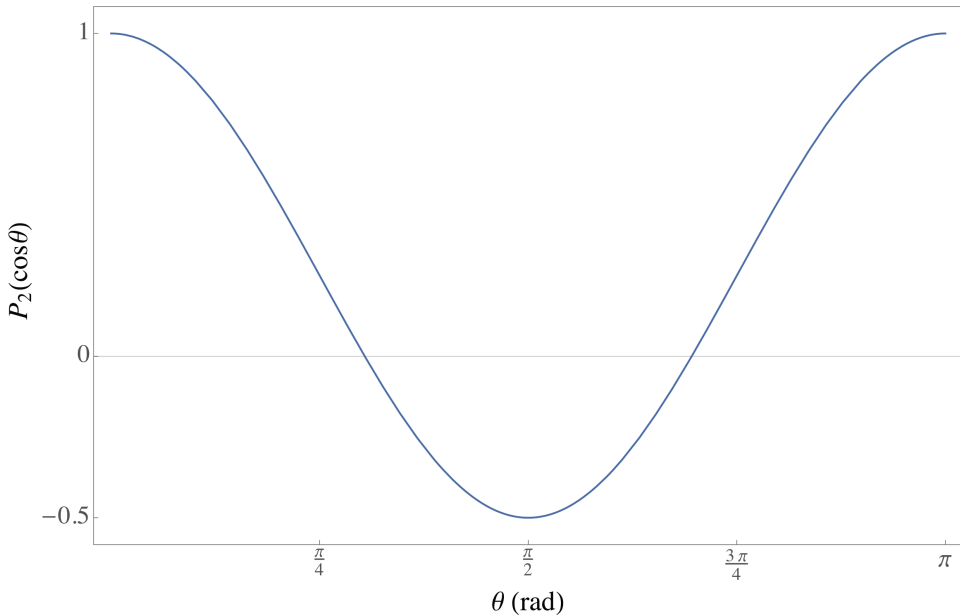


Figure 1.2: the second-order Legendre polynomial as a function of $\cos(\theta) = \vec{v} \cdot \vec{n}$ for $0 \leq \theta \leq \pi$

Creating dyadics from the eigenbasis, we can re-express the matrix in the eigen-representation:

$$\mathbf{Q} = Q^{(1)}\mathbf{e}^{(1)}\mathbf{e}^{(1)} + Q^{(2)}\mathbf{e}^{(2)}\mathbf{e}^{(2)} + Q^{(3)}\mathbf{e}^{(3)}\mathbf{e}^{(3)} \quad (1.6)$$

By construction, the original vectors are distributed symmetrically about the director, \vec{n} . From this it follows that \mathbf{Q} must also be uniaxially symmetric about \vec{n} [5]. This encourages us to decompose the uniaxial tensor into a parallel to the director projection and a perpendicular projection [5]. To do this, we let $\mathbf{e}^{(1)} = \vec{n}$ and recognize that by the uniaxial symmetry $Q_2 = Q_3 = Q_{\perp}$ and $Q_1 = Q_{\parallel}$ such that

$$Q_{ij} = Q_{\parallel}n_i n_j - Q_{\perp}(\delta_{ij} - n_i n_j) \quad (1.7)$$

The traceless condition gives $2Q_{\perp} = Q_{\parallel}$. Letting $Q_{\parallel} = 2S/3$ and grouping the like terms results in

$$Q_{ij} = S \left(n_i n_j - \frac{1}{3} \delta_{ij} \right) \quad (1.8)$$

In matrix form, we have that

$$\mathbf{Q} = \begin{pmatrix} 2S/3 & 0 & 0 \\ 0 & -S/3 & 0 \\ 0 & 0 & -S/3 \end{pmatrix} \quad (1.9)$$

The constant that parametrizes the eigenvalues, S , is called the scalar order parameter [1]. In the isotropic case, $Q_{ij} = 0$ and therefore $S = 0$. For the uniformly ordered case, since $\langle v_i v_j \rangle = n_i n_j$ from Equation 1.3 it follows that $S = 1$. We use the value (between zero and one) of the scalar order parameter to characterize the degree of alignment between the molecules [3].

The above computation reveals a procedure for determining the director and scalar order parameter. Given a sample of molecules, start by choosing an arbitrary coordinate system and compute Q_{ij} in that basis. Then transform into the eigenbasis of \mathbf{Q} by diagonalizing the matrix. The eigenvalue of greatest magnitude is $2S/3$ and the associated eigenvector is the director. From this construction, we can also

work out a useful relationship between the director and scalar order parameter. From Equation 1.8, we compute that $\vec{n} \cdot \mathbf{Q} \cdot \vec{n} = 2S/3$. Given Equation 1.3, it follows that

$$\vec{n} \cdot \mathbf{Q} \cdot \vec{n} = n_i \left\langle v_i v_j - \frac{1}{3} \delta_{ij} \right\rangle n_j = \left\langle n_i v_i n_j v_j - \frac{1}{3} \right\rangle = \left\langle (\vec{v} \cdot \vec{n})^2 - 1/3 \right\rangle \quad (1.10)$$

Letting θ describe the angle between molecular axis and \vec{n} and setting the above equation equal to $2S/3$ yields

$$S = \frac{3}{2} \left\langle (\cos \theta)^2 - 1/3 \right\rangle = \langle P_2(\cos(\theta)) \rangle \quad (1.11)$$

where we have substituted in the second-order Legendre polynomial, $P_2(x) = (3x^2/2 - 1/2)$ [3].

CHAPTER 2

Computer Simulation of Liquid Crystals

This chapter details the computational techniques and algorithms used to model the behavior of liquid crystals in this research. If we ignore the fluidity of a liquid crystal and focus only on the molecular orientation, we can divide the liquid crystal into small domains and model the average orientation of the molecules within each domain as a vector fixed to a three-dimensional lattice. We introduce the model for the energy interaction between neighboring molecules in this lattice model of the liquid crystal [6]. Since its introduction in 1979, model simulations of the nematic-isotropic transition have agreed closely with theoretical estimates and been pivotal in understanding the theory of liquid crystals. The remainder of the chapter is devoted to an in-depth overview of the core algorithm that many computer simulations of liquid crystals utilize: the Monte Carlo Method. We use the Metropolis Monte Carlo algorithm to randomly sample the configuration space of the liquid crystal. From this sampling data, we explain how to compute the expected values of macroscopic statistical properties (e.g. the energy and order parameter).

2.1 The Model

The model is a lattice-based model of a continuous liquid crystal composed of rod-like nematic particles. Based on Maier-Saupe mean field theory, the model neglects short range forces like the excluded volume effect and focuses on the alignment forces that control orientational ordering. Maier-Saupe theory prescribes an energy interaction between the i -th and j -th neighboring particles of the form

$$E_{ij} = -J_{ij}P_2(\cos(\theta_{ij}))$$

where θ_{ij} is the angle between the long axes of the neighboring molecules, $P_2(\cos(\theta_{ij})) = \frac{3}{2}(\cos(\theta_{ij})^2 - 1/3)$ is the second Legendre polynomial, and $J_{ij} > 0$ is a function of the distance between the molecules that falls off as $1/(r_i - r_j)^6$ [6]. If the molecules are perfectly aligned, $E_{\text{aligned}} = -J_{ij}$. If they are orthogonal, then $E_{\text{orthogonal}} = J_{ij}/2$. Since $J_{ij} > 0$, $E_{\text{aligned}} \leq E_{\text{orthogonal}}$ and the energy interaction favors alignment.

As discussed in Chapter 1, nematic liquid crystal molecules are ellipsoidal in shape and possess one long axis of symmetry. Simulating the liquid crystal necessitates keeping track of the position and orientation of each nematic molecule. In most computer languages, it is far easier to manipulate and store vectors than axes. For this reason, in the model, we choose to work with a vector that points along the long axis of the molecule rather than the axis itself. Note that given an axis, there are always two unit vectors parallel with it. For instance, the vectors $(1, 0, 0)$ and $(-1, 0, 0)$ are both parallel to the x-axis. Thus, when working with the model, we disregard the directions associated with the vectors and think of

them as being "headless".

To keep track of the orientational order in the liquid crystal, we use a rectangular lattice. At each lattice point, we store a vector that points along the long axis of the molecule that occupies that site. In the standard model, the orientations of the molecules are free to rotate, but the molecules themselves stay translationally fixed. This approach neglects the translational movement within the liquid crystal and focuses only on the orientational ordering. The model also confines energy interactions to between nearest neighbors only. As a consequence, the distance between interacting molecules is constant which fixes J_{ij} to a constant value. For simplicity, we work in energy units of ϵ where $E_{\text{aligned}} = -\epsilon$. The energy of the entire lattice as given by the Lebwohl-Lasher model is then

$$E = -\frac{\epsilon}{2} \sum_{\langle ij \rangle} P_2(\cos(\theta_{ij}))$$

where $\langle ij \rangle$ is a sum over each lattice site's six nearest neighbors and factor of 1/2 compensates for double counting each energy interaction [6].

For a given temperature, as we will explain in the next section, a Monte Carlo simulation produces the equilibrium state of the model. Once equilibrium has been reached, we can compute statistical properties of interest like the scalar order parameter, S , defined in Equation 1.11. For a given state, we compute S by following the procedure outlined in Chapter 1.3. First, we compute \mathbf{Q} as defined in Equation 1.3. The eigenvalue of \mathbf{Q} with the greatest magnitude is equal to $2/3S$. As shown in Chapter 1.3, the scalar order parameter vanishes in the high temperature isotropic limit and is unity in the perfectly aligned case. The Lebwohl-Lasher model simulation of the order parameter at different temperatures elucidates how the order parameter transitions from the ordered nematic phase to the disordered isotropic phase. In particular, the Lebwohl-Lasher model demonstrates that the system undergoes a first-order transition during which the order parameter changes discontinuously.

For example, Figure 2.1 shows data collected from Monte Carlo runs on a cubic lattice with edge length $L = 40$. The model started from isotropic initial conditions at low temperatures and nematic initial conditions at temperatures above T_{N-I} , the transition temperature. The initial conditions at the beginning of each temperature run were intentionally set far from the equilibrium state to demonstrate the robustness of the simulation. The Monte Carlo run at each temperature was conducted for 10,000 MC cycles with an average equilibration time of less than 1000 MC cycles. Once the system reached the equilibrium state, the order parameter and energy were recorded after each cycle. At the conclusion of the run, the mean order parameter was estimated by computing the mean of the set of equilibrated order parameter measurements. In Figure 2.1, The mean order parameter (plotted in green) clearly experiences a discontinuous jump at $E_{N-I} = k_B T_{N-I} \approx .9$

If we run the simulation at temperatures very close to the transition, we observe the system oscillate between two states with different order parameters. For instance, in Figure 2.2 a, we see for the cubic $L = 40$, the system oscillates within an energy per site range of $\Delta E_{\text{site}} = .3$. In comparison, we find that a MC run at 101% of the transition temperature equilibrates more smoothly with an energy spread of $\Delta E_{\text{site}} = .1$. The histogram of the order parameter measurements taken at each cycle reveals a bimodal distribution. The presence of a stable ordered and disordered state at the transition temperature indicates a first-order transition.

2.2 Monte Carlo Methods

Monte Carlo methods are a class of computer algorithms that involve randomly sampling from a distribution. This technique has found wide application across the sciences, finance, and engineering. In

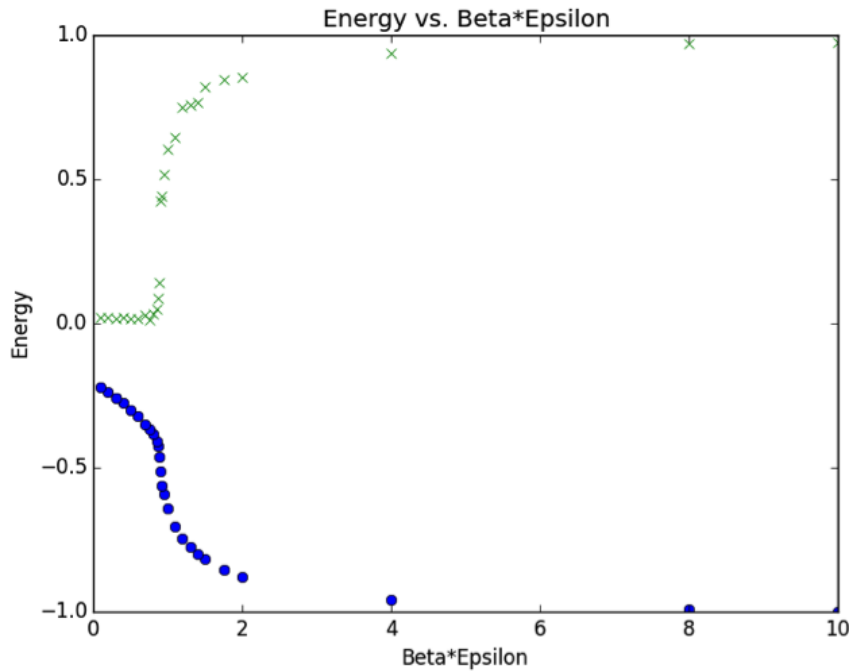


Figure 2.1: Plot of order parameter (green X) and the average energy (blue O) from data of 10,000 cycle Monte Carlo runs of a $L = 40$ cubic Lebwohl-Lasher model at various temperatures specified by $\beta = 1/(k_B T)$

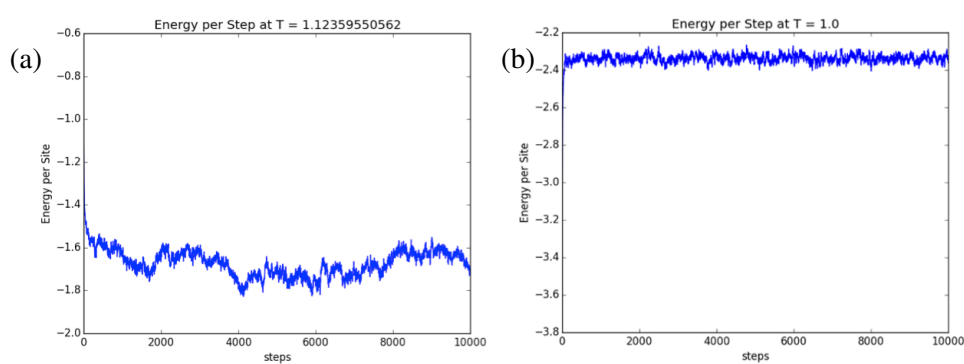


Figure 2.2: Plots of the energy per site for a 10,000 cycle Monte Carlo run on a $L = 40$ cubic Lebwohl-Lasher model at a) transition temperature and b) beneath the transition temperature

statistical physics, we use Monte Carlo methods to compute statistical quantities of interest for models with computationally large configuration spaces. The set of possible orientations of a single vector is simply S_2 , the surface of the two dimensional sphere. To specify a configuration state of the entire lattice requires listing a point on S_2 for each site on the lattice. Given N lattice sites, the set of all possible states, which is of size $(S_2)^N$, is called the configuration space.

The central idea behind Monte Carlo methods is that rather than analytically computing integrals over this entire configuration space, we approximate them via random sampling. We conduct this sampling by executing a random walk from microstate to microstate in the configuration space. For a more in-depth discussion of Monte Carlo methods see [7], [8], [9].

Let us start by considering a single-variable integral that we cannot compute analytically:

$$F = \int_{x_1}^{x_2} f(x) dx$$

We know from the mean value theorem for definite integrals that there exists a mean value, $c \in [x_1, x_2]$, such that

$$F = \int_{x_1}^{x_2} f(x) dx = (x_2 - x_1)f(c)$$

In general, although we know $f(c)$ exists, we do not know how to directly solve for it. Without more information about $f(x)$, one way to approximate the mean value $f(c)$ is to uniformly sample the interval $[x_1, x_2]$ and compute the average of the sample. Given N samples, $s_i \in [x_1, x_2]$, we compute

$$\langle f(x) \rangle_{\text{sample}} = \frac{1}{N} \sum_{i=1}^N f(s_i)$$

This sampling process yields the approximation [8] :

$$f(c) = \langle f(x) \rangle_{\text{sample}} + O(N^{-1/2})$$

In other words, in the high sampling limit, the mean of the sample set converges to the true mean. Equipped with this approximation for $f(c)$, we now simply multiply by $(x_2 - x_1)$ to arrive at an approximation of the integral. In short, this technique, called uniform sample integration, allowed us to approximate the definite integral via uniformly sampling the integrand.

In statistical mechanics, we are often interested in more complicated multivariable integrals over the phase space of a system. For instance, consider a liquid crystal at constant temperature, number of molecules, and volume. Suppose we are interested in a thermodynamic quantity such as the scalar order parameter, S . Given the canonical ensemble, we compute the ensemble average as

$$\langle S \rangle_{\text{ensemble}} = \frac{\int \exp(-\beta E(\Gamma)) S(\Gamma) d\Gamma}{\int \exp(-\beta E(\Gamma)) d\Gamma}$$

where $\beta = 1/kT$ and $d\Gamma$ is a differential element of phase space. We could uniformly sample both the numerator and denominator over the multidimensional phase space and arrive at an approximation to the integral in the same fashion as the one-dimensional case; however, we can improve the computational time and accuracy of approximation if we adopt a nonuniform sampling procedure [7]. In general, the integrand may vary widely over the phase space. If our sampling is unweighted, then we do not take advantage of this fact; we waste time sampling from regions that do not meaningfully contribute to the integral. This realization suggests that we weight our sampling, or in the language of Monte Carlo

methods, that we importance sample the phase space.

2.2.1 Metropolis algorithm

Going back to the ensemble average for S and identifying the canonical ensemble probability density,

$$\rho_{\text{NVT}}(\Gamma) = \frac{\exp(-\beta E(\Gamma))}{\int \exp(-\beta E(\Gamma)) d\Gamma}$$

we recognize that

$$\langle S \rangle_{\text{ensemble}} = \int \rho_{\text{NVT}}(\Gamma) S(\Gamma) d\Gamma$$

Rather than uniformly sample the integrand, importance sampling capitalizes on the fact that the magnitude of the integrand depends on the magnitude of $\rho_{\text{NVT}}(\Gamma)$. Therefore, we should weight the sampling procedure so that we prioritize microstates from regions of the configuration space where $\rho_{\text{NVT}}(\Gamma)$ is large. The intuitive way to achieve this is just to select microstates from the configuration space by sampling the probability distribution $\rho_{\text{NVT}}(\Gamma)$.

Sampling the probability distribution $\rho_{\text{NVT}}(\Gamma)$ N times generates a set of microstates $\{\Gamma_1, \Gamma_2, \dots, \Gamma_N\}$. In the $N \rightarrow \infty$ limit, we expect that the frequency that a given microstate occurs should be proportional to $\rho_{\text{NVT}}(\Gamma)$. In importance sampling terminology, we say that the set $\{\Gamma_1, \Gamma_2, \dots, \Gamma_N\}$ has $\rho_{\text{NVT}}(\Gamma)$ as its limiting distribution. Methods of generating a set with a given limiting distribution generally rely on the technology of Markov chains.

A Markov chain is a sequence of microstates sampled from the configuration space such that the probability distribution of Γ_n only depends on Γ_{n-1} . As a consequence, the method of generating the n -th state in the sequence only depends on the most recent state in the sequence and is independent of the rest of the preceding chain. This is known as the "memoryless" property of Markov chains [8].

To keep track of the states occurring in the Markov chain, at each step we compute a distribution vector ρ . For each element

$$\rho_n = \frac{\text{# of occurrences of } \Gamma_n \text{ in chain}}{\text{length of chain}}$$

For instance, a Markov chain for five flips of a fair coin (with $\Gamma_1 = \text{heads}$ and $\Gamma_2 = \text{tails}$) might be $\{\Gamma_1, \Gamma_2, \Gamma_1, \Gamma_2, \Gamma_2\}$ with the corresponding distribution vector $\rho = (2/5, 3/5)$. Assuming the coin is fair, we can write down a transition matrix, π , that describes how the distribution vector changes after each flip:

$$\pi = \begin{pmatrix} .5 & .5 \\ .5 & .5 \end{pmatrix}$$

where π_{mn} is the probability of transitioning from Γ_m to Γ_n , in this case 50%. Flipping the coin and generating the next state to add on to the Markov chain is equivalent to applying the transition matrix to the distribution vector. Therefore, we expect that repeated operation of π on ρ will limit to $\rho_{\text{limit}} = (.5, .5)$. As a consequence, we note that the limiting distribution must be an eigenvector of π with eigenvalue of unity.

Given that we are modeling a liquid crystal, we also require that the Markov chain satisfy the following properties:

- Condition of Detailed Balance: the frequency of the $\Gamma_n \rightarrow \Gamma_m$ transition is the same as the frequency of $\Gamma_m \rightarrow \Gamma_n$ transition. We enforce this by requiring

$$\rho_m \pi_{mn} = \rho_n \pi_{nm}$$

The physical motivation is that in equilibrium any specific transition should be equally likely as the reverse transition. If the frequencies were not equal, then the system would move out of equilibrium and spend more time in the favored high frequency state. Since this is a contradiction, the transition frequencies must be equal at equilibrium.

- Ergodic Condition: there exists a non-zero probability multiple step transition from one state to any other. Given any initial state of the liquid crystal in the lab, if we waited long enough (theoretically an infinite amount of time), we would observe it traverse the entire configuration space. In other words, the entire configuration space is accessible from any starting state. Therefore, when we construct the Markov chain we need to ensure that there exists a multiple-step chain connecting any two states.

In the case of the liquid crystal, we do not explicitly know the transition matrix, but we do know the limiting distribution since by design we have $\rho_{\text{limit}}(\Gamma_i) = \rho_{\text{NVT}}(\Gamma_i)$. Using this limiting distribution, we construct a transition matrix and a step generation procedure using the Metropolis algorithm [7],[9]:

Given states Γ_n and Γ_m , we compute the $\Gamma_m \rightarrow \Gamma_n$ transition element as

$$\pi_{mn} = \begin{cases} \alpha_{mn} & \text{if } \rho_{\text{NVT}}(\Gamma_n) \geq \rho_{\text{NVT}}(\Gamma_m) \\ \frac{\rho_{\text{NVT}}(\Gamma_n)}{\rho_{\text{NVT}}(\Gamma_m)} \alpha_{mn} & \text{if } \rho_{\text{NVT}}(\Gamma_n) < \rho_{\text{NVT}}(\Gamma_m) \end{cases}$$

where α is a symmetric matrix with rows that sum to unity (i.e., a stochastic matrix). There is freedom in choosing the α matrix, but some choices are more efficient than others depending on the specifics of the model. Formally, any matrix that is stochastic, symmetric and produces a balanced and ergodic chain is sufficient.

To get a better sense of the algorithm, consider the instructive example of a Markov model consisting of N states that all share an identical energy so that for all i , $\rho_{\text{NVT}}(\Gamma_i)$ is fixed. In this case, we have $\pi = \alpha$ and the simplest choice for α is simply $\alpha_{mn} = 1/N$. Given any state Γ_m , it will transition with equal probability to any other state (including itself). If we now consider a model with nonidentical energy states, we can still implement the intuitive choice for α , but we also make transitions that raise the energy less likely: we diminish the initial probability stemming from α_{mn} by multiplication with $\frac{\rho_{\text{NVT}}(\Gamma_n)}{\rho_{\text{NVT}}(\Gamma_m)} < 1$. This also follows from the detailed balance condition: $\rho_m \pi_{mn} = \rho_n \pi_{nm}$. Suppose that for Γ_n and Γ_m , $\rho_{\text{NVT}}(\Gamma_n) < \rho_{\text{NVT}}(\Gamma_m)$, then $\pi_{nm} = \alpha_{nm}$. Detailed balance and the symmetric property of α produce $\pi_{mn} = (\rho_n / \rho_m) \alpha_{mn}$ as desired.

The flexibility in specifying α allows the algorithm to be tailored to the problem at hand. For the liquid crystal model it is computationally easier to transition between related states than to randomly generate an entirely distinct state each transition. In fact, the computationally lightweight solution is to transition by randomly rotating a single molecule in the lattice: α_{mn} is then non-zero only if Γ_m are Γ_n are identical except at a single site.

2.2.2 Liquid Crystal Metropolis Implementation

In the standard implementation of the Lebwohl-Laser model, a Markov step consists of a rotation move that rotates a vector at a single site in the lattice. Motivated by our later investigation of the multispecies model, we will also consider exchange moves that swap the orientations of two molecules in the lattice. We will first detail the implementation of the Metropolis algorithm for rotation moves.

For rotation moves, the algorithm starts by selecting a site at random in the lattice. Before the rotation let Γ_m be the current microstate of the system. First, we select a site at random from the N possible sites

in the lattice. We then sample a uniform probability distribution over a sphere to generate a random step in the θ and ϕ coordinates of the molecule at that site. This sampling process produces a trial final state Γ_n . If $\rho_{\text{NVT}}(\Gamma_n) \geq \rho_{\text{NVT}}(\Gamma_m)$, then we accept the move since $\pi_{mn} = \alpha_{mn}$ and no further computation is necessary. If $\rho_{\text{NVT}}(\Gamma_n) < \rho_{\text{NVT}}(\Gamma_m)$, we have to accept the trial move according to the probability:

$$\frac{\rho_{\text{NVT}}(\Gamma_n)}{\rho_{\text{NVT}}(\Gamma_m)} = \frac{\exp(-\beta E_n) d\Omega^n dr^n}{\exp(-\beta E_m) d\Omega^m dr^m} = \frac{\exp(-\beta E_n) \sin(\theta_n)}{\exp(-\beta E_m) \sin(\theta_m)} = \frac{\sin(\theta_n)}{\sin(\theta_m)} \exp(-\beta \Delta E_{nm})$$

Note that we multiply by the differential element of phase space to convert the probability density to a probability. Since the states differ by the rotation of a single molecule, the phase elements are not equal. In order to accept the move with probability $P = \sin(\theta_n)/\sin(\theta_m) \exp(-\beta \Delta E_{nm})$, we generate a random number, x , in the range $[0, 1]$ and accept the move if $x \leq P$.

The algorithm we implement in our simulations is a slight variant of the one presented above. Instead of incorporating the ratio of the $\sin(\theta)$'s probability factor into the ρ_n/ρ_m step, we modify the initial α transition step. Since $d\cos(\theta) = \sin(\theta)d\theta$, we randomly step in $\cos(\theta)$ and ϕ rather than in θ and ϕ . The full pseudocode of this algorithm is presented below:

Algorithm 1 Rotation Move Step of Metropolis algorithm

```

1: select a lattice site at random
2: generate trial rotation move at selected lattice site:
3:   uniformly sample  $\delta\phi$  from  $[\delta\phi_{\min}, \delta\phi_{\max}]$ 
4:    $\phi = \phi + \delta\phi$ 
5:   uniformly sample  $\delta \cos(\theta)$  from  $[-\delta \cos(\theta)_{\min}, \delta \cos(\theta)_{\max}]$ 
6:    $\cos(\theta) = \cos(\theta) + \delta \cos(\theta)$ 
7: compute energy of trial state  $E_{\text{trial}}$ 
8: if  $E_{\text{trial}} \leq E$  then
9:   accept the trial move
10: else  $E_{\text{trial}} > E$ 
11:   generate random number  $x$  by uniformly sampling  $[0, 1]$ 
12:   if  $x \leq \exp(-\beta(E_{\text{trial}} - E))$  then
13:     accept the trial move
14:   else
15:     reject trial move
16:   end if
17: end if
```

Note that in the rotation algorithm, we parametrize the range in which the random steps in ϕ and $\cos(\theta)$ can vary. The parameters are dynamically optimized over the course of the simulation with the goal of maintaining a 50% acceptance ratio. For illustration, let's say that the system is not yet in equilibrium. Restricting the random steps to be very small would result on average in a high acceptance ratio since trial moves that result in a large unfavorable energy shift are unlikely. Because each cycle only results in slight changes, the model will equilibrate slowly. On the other hand, if we allow for the full possible random step ranges, each trial move dramatically changes the local energy. Significant movement often disturbs the local ordering and results in a sizable increase in energy. As a consequence, these moves are unlikely to be accepted and computation time is wasted generating rejected moves; hence the need to generate moves that are likely to be both accepted and to meaningfully move the system towards equilibrium. There is no proof that a 50% acceptance ratio produces these ideal results, but the number

has an attractive intuitive appeal and serves as a heuristic [9].

For exchange Monte Carlo moves, the algorithm is even simpler. We do not have to be concerned with the $\sin(\theta)$ factor: consider the total angular integration element $d\Omega^n = \prod d\Omega_i$ where the product runs over all the molecules in the lattice. Exchanging two molecules reorders but does not change the value of the product, so that $d\Omega^n/d\Omega^m = 1$. An exchange move begins by selecting a pair of trial adjacent molecules to interchange. The α matrix gives the probability of uniformly selecting any two sites in the lattice. We also allow for the selection of the same site twice (i.e., there is a nonzero probability of returning to the same state). Let there be d lattice sites. Then,

$$\alpha_{nm} = \begin{cases} 1/(d\text{Choose}2 + d) & \text{if } \Gamma_n \text{ and } \Gamma_m \text{ are identical except for the interchange of two molecules} \\ 0 & \text{otherwise} \end{cases} \quad (2.1)$$

The interaction energy between the molecules and their neighbors is calculated. The molecules are then exchanged and the total energy of this new configuration is calculated. If $E_{\text{trial}} \leq E$, the move is accepted. If $E_{\text{trial}} > E$, the move is accepted with probability

$$\frac{\rho_{\text{NVT}}(\Gamma_n)}{\rho_{\text{NVT}}(\Gamma_m)} = \frac{\exp(-\beta E_n)}{\exp(-\beta E_m)} = \exp(-\beta \Delta E_{nm})$$

To ease computation, it is helpful to calculate ΔE_{nm} by computing the energy interactions of only the trial molecules with their neighbors. The rest of the lattice energy is invariant under the exchange move and therefore does not have to be recalculated. The full pseudocode of the exchange move algorithm is presented in Algorithm 2.

The necessity of the exclusion clauses is apparent after considering an exchange move between a pair of neighboring molecules. The change in energy does not depend on the interaction energy of the pair itself.

The above presentation focused on the formal aspects of the Monte Carlo method as a means to importance sample via a Markov chain process. In modeling liquid crystals, it is also helpful to have a more intuitive and thermodynamic picture of the Monte Carlo procedure. We know that the liquid crystal sample is in thermal equilibrium with a heat bath at fixed temperature. If we were able to cool the temperature of the heat bath to absolute zero, then the system would transition to the minimum energy microstate. For the Lebwohl-Lasher model, we know this results in the aligned nematic phase. The presence of the heat bath delivers energy "kicks" to the liquid crystal which alter the molecular alignment. Moves that lower the energy of the liquid crystal can be viewed as the result of the system "internally" sinking to its energy minimum. Equilibrium is reached when the opposing tendencies balance out. This framework does not capture the statistical details of the Monte Carlo method, but is often helpful to keep in mind when running simulations.

Algorithm 2 Exchange Move Step of Metropolis algorithm

```

1: select adjacent site pair from the lattice at random:
2:   uniformly sample  $(x, y, z)$  coordinates from  $([1, L], [1, W], [1, H])$ 
3:   site A  $\rightarrow (x, y, z)$ 
4:   uniformly sample  $(u, v, w)$  coordinates from  $([1, L], [1, W], [1, H])$ 
5:   site B  $\rightarrow (u, v, w)$ 
6: compute exchange energy  $\Delta E_{nm}$ 
7: calculate,  $E_A$ , the energy of molecule A with its neighbors (excluding site B if present)
8: calculate,  $E_B$ , the energy of molecule B with its neighbors (excluding site A if present)
9: calculate,  $E_{Aswap}$ , the energy of molecule A with molecule B's neighbors (excluding itself if
   present)
10: calculate,  $E_{Bswap}$ , the energy of molecule B with molecule A's neighbors (excluding itself if
    present)
11:  $\Delta E_{nm} = (E_{Aswap} + E_{Bswap}) - (E_A + E_B)$ 
12: if  $\Delta E_{nm} \leq 0$  then
13:   accept the trial move
14: else  $\Delta E_{nm} > 0$ 
15:   generate random number,  $x \in [0, 1]$ 
16:   if  $x \leq \exp(-\beta\Delta E_{nm})$  then
17:     accept the trial move
18:   else
19:     reject trial move
20:   end if
21: end if

```

CHAPTER 3

Defect Structures

This chapter details the formation of defect structures by fixing the orientations of molecules on the lattice boundary. We begin by summarizing the stability of defect structures using the language of algebraic topology. In particular, we employ homotopy theory to characterize 180° disclination lines in the nematic liquid crystal. We then provide a brief survey of the current experimental techniques utilized to induce these defects. Following this, we review the boundary conditions known to produce wedge disclination loops (WDL's) and pairs of disclination lines. We propose generalizations on WDL boundary conditions that provide the suitable boundary conditions to construct any two-dimensional, smooth, closed curve from defects. We demonstrate how, through dynamic adjustment of the boundary conditions, we can deform and evolve these defect structures. Taking inspiration from Winoker's work, we establish boundary conditions that successfully thread disclination lines through wedge disclination loops.

3.1 Topology of Defects

Tools from algebraic topology and homotopy theory provide the natural mathematical framework to describe defects in liquid crystals. Using the topological point of view, the stability of defects and the combination laws for defects can be rigorously computed.

The point of departure of the topological treatment is mapping the physical orientations of the molecules to the more abstract order-parameter space. Order-parameter space is a space in which each element is in 1-1 correspondence with a possible orientation of a nematic molecule. In our Lebwohl-Lasher model, we specify a molecule's orientation with a vector. At first glance, this suggests that each possible orientation of the vector could be mapped to a point on the surface of S^2 , the ordinary two-dimensional sphere. The vector description, however, is merely a stand-in for the molecular axis of the ellipsoidal molecule. Two anti-parallel vectors represent the same molecular orientation, but antipodal points on S^2 are not identical. As a consequence, the orientation-parameter space (from here on referred to as R) for nematics is S^2 with an additional identification of antipodal points. This space is also equivalent to the set of lines going through the origin in three-dimensional space - known as the 3D real projective plane and notated as RP^2 .

To map the molecular orientations in a region of the liquid crystal to paths in R , we first superimpose a closed contour, C , on the region of interest. Traveling clockwise around the countour, we map each $x \in C$ to $y \in R$, where y corresponds to the orientation of the molecule located at x . This procedure generates a mapping $f : C \rightarrow R$. For the case of two-dimensional spins, the order-parameter space is simply the circle. Two planar spin patterns are shown in Figures 3.1 and 3.2. For the perfectly ordered pattern, traversing around the circle starting from the base point A maps to a single point in R . For the

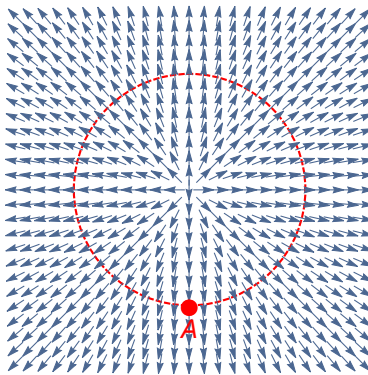


Figure 3.1: A radial pattern of planar spins and a circular contour with base point A. The mapping specified by this pattern generates a path in $R = S^1$ with a winding number of one.

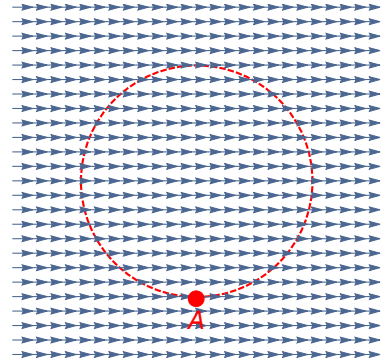


Figure 3.2: The perfectly ordered state of planar spins and a circular contour with base point A. The mapping specified by this pattern maps to a single point on $R = S^1$ and thus has a winding number of zero.

radial pattern, a path around the circle in physical space maps to a full loop around $R = S^1$. Thermal excitations cause the molecules to jiggle and rotate. These excitations alter and deform the mapping to R . Because the underlying physics governing the excitations evolves continuously in time, the deformations to the paths in R must also be continuous.

Mappings that generate contours in R that can be continuously deformed (i.e., no gluing or tearing operations) into one another are considered homotopic. For the 2-D spin example, maps that generate paths in R with the same winding number are homotopic to each other. This allows us to construct equivalence classes of homotopic maps and enumerate them by the winding number of a representative map from the class. Such a classification scheme provides insight into how molecular orientation patterns evolve. For instance, we can use this technology to compute how regions with different orientation patterns interact and combine. In the 2-D spin case, if two patterns individually generate loops in R with winding number a and b , then the pattern that results from their combination will produce an R -loop with winding number $a + b$. In other words, the composition of maps from different equivalence classes behaves like the integers under addition. This group structure exhibited by the equivalence classes (of homotopic maps) is known as the fundamental group of R and is written as $\pi_1(R)$ [10]. For the 2-D spins, we have thus found that $\pi_1(S^1) = \mathbb{Z}$. For the nematic case, the fundamental group has a less familiar structure and requires a more involved computation.

To compute the fundamental group of the nematic liquid crystal, we rely on a deep connection between the symmetries exhibited by R and the fundamental group. Describing the symmetries of R requires a brief introduction to the mathematics of continuous groups. In a continuous group, we can construct infinite sequences of elements that converge to elements within the group. Given two sequences of elements $\{a_n\}, \{b_n\} \in G$ that converge to elements a and b in G , the group is continuous if $\{a_n b_n^{-1}\}$ converges to $ab^{-1} \in G$ [11]. Two elements a, b are connected if there exists a continuous sequence $\{a_n\}$ such that $a_0 = a$ and a_n converges to b . In more geometrical terms, we consider this sequence to represent a continuous path that traverses elements in the group starting at a and terminating at b . It is relatively easy to show that sets of elements that are mutually path-connected form subgroups. These subgroups are termed the connected components of the group [11]. In particular, let G_0 be the subgroup that contains all elements connected to e , the identity element.

Given an order-parameter space, we introduce a transformation group, G , that acts transitively on R . By this we mean that given $r_1, r_2 \in R$, we can act with $g \in G$ such that $gr_1 = r_2$ [10]. For the case of

2-D spins, $R = S^1$ and we will let $G = \text{SO}(2)$. In the familiar Cartesian parametrization of S^1 , for each $r \in S^1$, there exists (x_1, x_2) such that $x_1^2 + x_2^2 = 1$. This parametrization of R suggests that we introduce the matrix representation of the transformation group, $\text{SO}(2)$. We transform from r to r' with a 2×2 matrix $M \in \text{SO}(2)$ such that $x'_i = M_{ij}x_j$. If we concern ourselves with the set of transformations that leave the order-parameter invariant for the ordered phase, we find that these transformations form a subgroup. This subgroup of G , called the isotropy group, is formally defined as $H = \{gf = f \mid g \in G\}$, where $f \in R$ is the order-parameter for the perfectly ordered phase [11]. For the planar spins, the fully ordered pattern is displayed in Figure 3.2 and H consists solely of the identity element.

In the nematic case, both G and H have a different structure. To transform from a given molecular axis to any other in three dimensions, we set $G = O(3)$. In the ordered phase, reflections about lines orthogonal to the molecular axis as well as rotations about the molecular axis itself leave the order-parameter invariant. The isotropy group formed by these transformations is known as the point-group D_∞ [10].

In the conventional physics language, G is regarded as the symmetry group of the disordered phase and H as the symmetry group of the ordered phase. From the algebraic properties of G and H , we can surprisingly extract the structure of R itself. The quotient group G/H is in fact isomorphic to R ! The proof of this relationship is beyond the scope of this report, but we refer interested readers to [12] and [10] for more detailed discussions that this overview draws heavily from. We will illustrate this relationship with two examples. First, we remind readers that the quotient group is defined as the group of cosets of H in G . Formally, $G/H = \{gH \mid g \in G\}$ and we choose the left coset convention whereby $gH = \{gh \mid h \in H\}$.

Applying this to the planar spins, we find that $\text{SO}(2)/e = \text{SO}(2)$ since the cosets of e are simply the original group elements. We note that $\text{SO}(2)$ can be parametrized by a single rotation angle, ϕ , that specifies a transformation. For example, in the canonical parametrization, $M(\phi) \in \text{SO}(2)$ is given by

$$M(\phi) = \begin{pmatrix} \cos \phi & -\sin \phi \\ \sin \phi & \cos \phi \end{pmatrix}$$

By mapping $M(\phi)$ to the point a sector-angle ϕ away from an (arbitrary) reference location on S^1 , we can construct an isomorphism between $\text{SO}(2)$ and S^1 [11]. Thus, we have recovered $R = S^1$ for the planar spins using the G/H construction. A similar computation for the nematic case reveals that $\text{SO}(3)/D_\infty = RP^2$ [12].

With these constructions under our belt, we can invoke a powerful theorem from algebraic topology that relates the quotient group to the fundamental group. Namely, given a simply-connected, continuous group G with subgroup H , the quotient group H/H_0 is isomorphic to $\pi_1(G/H)$ [10]. The quotient group approach has two appealing features: it characterizes the order-parameter space in terms of the symmetries of the ordered and disordered phases and provides a means to compute the algebraic structure of the defect combination laws.

In the following computation, we apply this construction to solve for the fundamental group for the nematics. As discussed before, $\text{SO}(3)$ contains transformations that can take any $r \in RP^2$ to any other $r' \in RP^2$. Unfortunately, we cannot apply the above theorem with $G = \text{SO}(3)$ because $\text{SO}(3)$ is not simply-connected [11]. To see this, we invoke the parametrization of $\text{SO}(3)$ as a ball of radius π with antipodal points identified. A given point in the ball specifies a rotation about the axis connecting the point to the origin. The rotation angle about this axis is given by the distance between that point and the origin. Antipodal points on the surface of the ball are identified because π and $-\pi$ rotations about any axis produce the same physical transformation. For G to be simply connected, all loops on G must be homotopic to the constant loop. Visually, this implies that we can continuously deform and shrink any

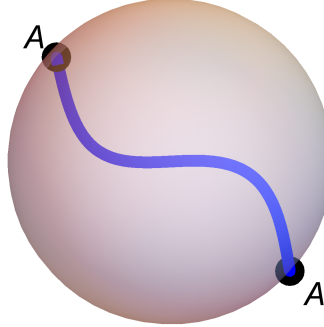


Figure 3.3: A visualization of $SO(3)$ as a unit ball with antipodal surface points identified. The path (in blue) connecting two identified points and passing through the interior of the ball cannot be continuously shrunk to a point with the endpoints fixed. This shows that $SO(3)$ is not simply connected.

loop down to a point. Consider a loop originating on the surface of the ball, then coursing through the ball's interior, and resurfacing at the point antipodal to the starting location. Such a loop is displayed in 3.3. With the endpoints fixed, it is intuitively clear that we cannot contract this loop to a point. This loop demonstrates that $SO(3)$ is not simply-connected [10].

We must make the alternate choice of $G = SU(2)$, which is simply-connected and contains all the necessary transformations ($SO(3) \subset SU(2)$). The simply-connected nature of $SU(2)$ is clear from the fact that it is diffeomorphic to S^3 [11]. We will represent $SU(2)$ with the Pauli matrix parametrization familiar to students of quantum mechanics. Let $\vec{\sigma}$ be the vector constructed from the Pauli matrices such that

$$\sigma_x = \begin{pmatrix} 0 & 1 \\ 1 & 0 \end{pmatrix}, \quad \sigma_y = \begin{pmatrix} 0 & -i \\ i & 0 \end{pmatrix}, \quad \sigma_z = \begin{pmatrix} 1 & 0 \\ 0 & -1 \end{pmatrix}$$

A rotation about an arbitrary axis, \hat{n} , by an angle $0 \leq \theta \leq \pi$ is represented by a matrix $U(\hat{n}, \theta) \in SU(2)$ such that

$$U(\hat{n}, \theta) = \exp\left(\frac{i\theta}{2}\hat{n} \cdot \vec{\sigma}\right)$$

Working in this representation, we now compute the isotropy subgroup. For simplicity, we orient $R = RP^2$ such that the reference-ordered axis points along the z-axis. Rotations about the z-axis will thus leave the order-parameter invariant from which it follows that $U(\vec{z}, \theta) \subset H$. Reflections about lines orthogonal to the z-axis will also preserve the order-parameter. Any such reflection can be decomposed into a rotation by π about the y-axis followed by a rotation about the z-axis. We label this set of reflections as $V(\vec{z}, \theta) = U(\vec{z}, \theta)U(\vec{y}, \pi) \subset H$. Therefore, H is the union of $V(\vec{z}, \theta)$ and $U(\vec{z}, \theta)$. Explicitly computing the forms of $V(\vec{z}, \theta)$ and $U(\vec{z}, \theta)$ reveals that the subgroups are not connected. For example, we first note that $U(\vec{z}, 0) = I$ and therefore $U(\vec{z}, \theta)$ is the identity component, H_0 . However,

$$V(\vec{z}, \theta) = U(\vec{z}, \theta)U(\vec{y}, \pi) = \exp\left(\frac{i\theta}{2}\vec{\sigma}_z\right)\exp\left(\frac{i\pi}{2}\vec{\sigma}_y\right) = \begin{pmatrix} 0 & e^{i\theta/2} \\ -e^{i\theta/2} & 0 \end{pmatrix}$$

No possible path starting at $V(\vec{z}, \theta)$ (which we could parametrize in terms of a sequence $\{\theta_n\}$) could possibly lead to the identity element. Since the connected components are disjoint, we arrive at the result that the other connected component of H is given by $H_1 = V(\vec{z}, \theta) = H_0 U(\vec{y}, \pi)$ [10]. Therefore, the quotient group, H/H_0 is a two-element group consisting of $\{e, U(\vec{y}, \pi)\}$. Relying on the fact that $\sigma_y^2 = 1$, computation reveals that

$$\begin{aligned} U(\vec{y}, \pi) &= \exp\left(\frac{i\pi}{2}\sigma_y\right) = \sum_{n=0} \frac{(i\pi/2)^n}{n!} \sigma_y^n \\ &= \left(\sum_{n,even} \frac{(-\pi/2)^n}{n!} \right) I - i \left(\sum_{n,odd} \frac{(-\pi/2)^n}{n!} \right) \sigma_y \\ &= \cos(\pi/2)I + i \sin(\pi/2)\sigma_y = i\sigma_y \end{aligned}$$

In summary, $H/H_0 = \{e, i\sigma_y\}$. All $O(2)$ groups are isomorphic to $Z_2 = \{0, 1\}$ [11]. We have thus found that for nematics, $\pi_1(R) = \pi_1(SU(2)/H) = H/H_0 = Z_2$. The non-removable pattern corresponding to $i\sigma_y$ is labeled a defect because it cannot continuously be deformed into the perfectly ordered pattern. Algebraically, this is given by a path that connects elements in H_0 to $H_0 i\sigma_y$ (e.g., the path that connects e to $i\sigma_y$). Given that $U(\vec{y}, \theta) = \cos(\theta/2)I + i \sin(\theta/2)\sigma_y$, we could parametrize this path by simply letting θ go from π to zero. In physical space, as we loop around the circle superimposed on the molecules, this would result in a rotation of the molecular axis by π . The defect pattern this produces is termed a 180° point defect displayed in Figure 3.4, which is the only stable point defect found in 3D nematics [12].

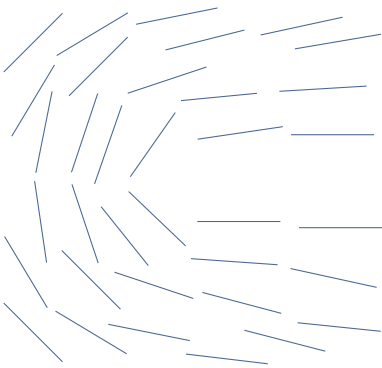


Figure 3.4: A planar 180° point defect in a 3D nematic sample. The point defect is stable and cannot be removed via local surgery. A disclination line can be visualized by repeating the pattern along the dimension extending out of the page

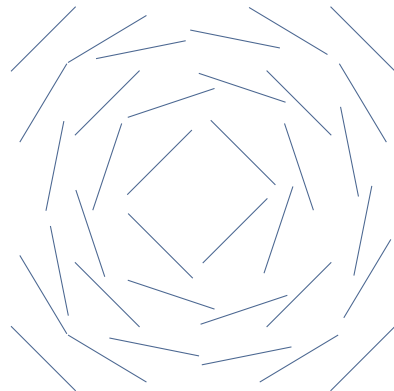


Figure 3.5: A planar 360° point defect in a 3D nematic. By rotating the molecules out of the page, the pattern can be smoothly deformed into a perfectly ordered sample with director normal to the plane of the page

Upon first inspection, it may seem that a 360° point defect as shown in Figure 3.5 would also be stable in the 3D nematic. Local surgery in the plane of the page cannot remove this defect, but we can continuously relax the pattern to the ordered state by rotating the molecules out of the page. One can visualize placing a hand along a radial line and lifting the molecules while sweeping the radial line about the origin. Such a procedure continuously produces a uniformly ordered state with the director out of the page.

Why does this fail for the 180° point defect? Repeating the lift-and-sweep motion about the core of the defect deforms the pattern discontinuously. The end of the molecule that is lifted out of the page at the

start of the lift-and-sweep motion is reversed after a full revolution. As a result, there is no continuous means for the defect to escape to the ordered state. The removal of the 180° point defect is only possible if it is destroyed via combination with another 180° point defect. We can visualize this process by combining the defect shown in Figure 3.4 with a 180° rotated copy of itself. This would produce a 360° point defect which can then escape to the ordered state. Mathematically, this result is clear from the combination law for Z_2 (direct computation also reveals that $H_0 i \sigma_y H_0 i \sigma_y = H_0$).

Due to topological reasons discussed in [13], singular instances of 180° point defects are not found within the nematic. Rather, 180° point defects are always located adjacent to other point defects. A sequence of these point defects is referred to as a disclination line which is depicted in Figure 3.6. Disclination lines cannot terminate in the bulk and therefore must connect the boundaries of the nematic sample or form a closed curve.

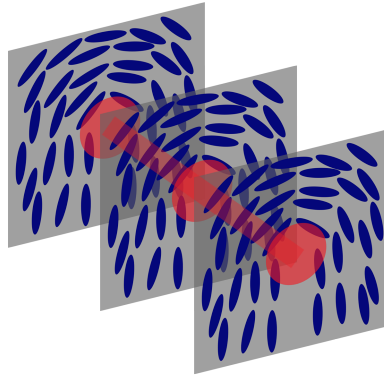


Figure 3.6: a depiction of a disclination line (highlighted in red) that is composed of planar 180° point defects

3.2 Defect Detection

To detect the presence of 180° disclination lines in the Lebwohl-Lasher model of Chapter 2.1, we implement the defect search algorithm of Zapotocky et al. [14]. The algorithm identifies defect structures by looping around unit square contours in the lattice and tracking how the molecular axis rotates [14]. If the molecular axis undergoes a 180° rotation, then a defect is present due to the topological argument presented in the previous section. Instead of charting out the path in RP^2 , it is easier to track the movement of an intersection point of the molecular axis with the sphere. If the molecular axis is rotated by 180° , then this intersection point will move across the surface of the sphere such that the initial and final states are separated by an arc sector angle of 180° . Given the discrete nature of the model, we cannot continuously map out the intersection point's path on the sphere. Instead, we must statistically infer it from the four vectors located at each vertex of the square contour.

Given a unit square contour, we enumerate the vertices in a clockwise fashion and let \vec{v}_i be the vector located at the i -th vertex ($i = 1, 2, 3, 4$). The point located at the tip of \vec{v}_1 marks the initial intersection point of the molecular axis with the sphere. Tracking the other intersection point specified by $-\vec{v}_1$ would also work, but utilizing the \vec{v}_1 point is one less step. Proceeding to the second vertex, the molecular axis intersects the sphere at two points specified by \vec{v}_2 and $-\vec{v}_2$. To which of these two intersection points was the initial \vec{v}_1 intersection point rotated?

Smaller rotations are energetically favorable and more probable. Therefore, we choose the intersection point that is closest to \vec{v}_1 . This process is then repeated for the third and fourth vertex intersection points.

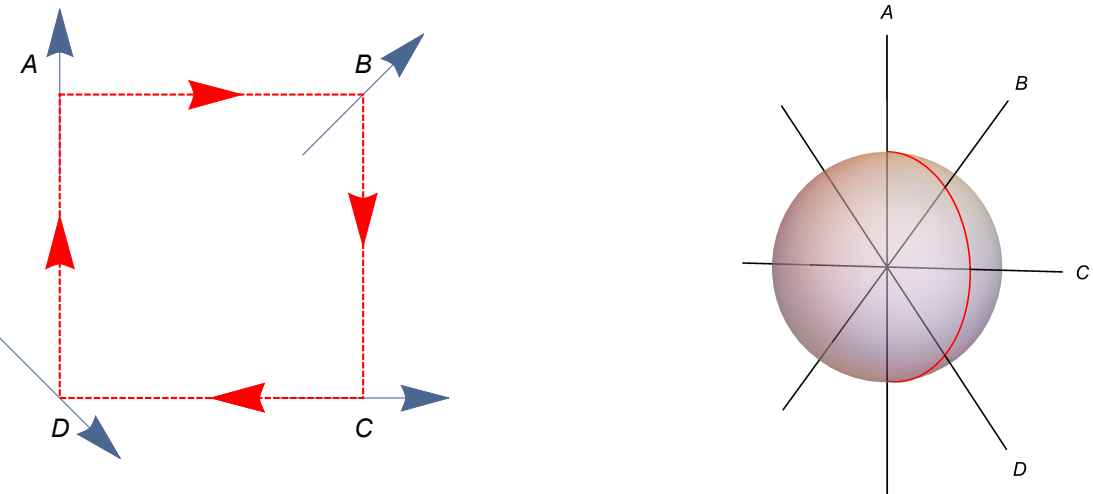


Figure 3.7: The core of a disclination line represented in the lattice model. Blue vectors point along the molecular axis of the LC molecule. The red, dashed path is the contour used to track the rotation of the molecule.

Figure 3.8: The inferred path of an intersection point of the molecular axis with the sphere for the contour in Figure 3.6.

Finally, we compare the fourth intersection point to the first intersection points. If they are separated by $\theta < 90^\circ$, we conclude that the molecular axis did not experience a 180° rotation. If $\theta \geq 90^\circ$, we conclude that a 180° rotation did occur and a disclination is present. Computationally, we use the dot product to determine the distances between the vectors. If the dot product of two vectors is negative, then the molecules are separated by $\theta > 90^\circ$.

A sample contour and mapping to the sphere for a defect core are presented in Figures 3.6 and 3.7. The coordinates at the center of the square contour are recorded as the location of a defect core. This search algorithm is executed on all the unit square contours in the lattice, which accounts for defects located in the XY, YZ, and XZ planes.

3.3 Experimental Defect Induction Techniques

Various techniques exist to experimentally induce the stable line disclinations discussed in the prior section. Tkalec et al. pioneered a method for producing arbitrarily complex, knotted defects in a chiral nematic liquid crystal (CNCL) with suspended spherical colloids [15], [16]. The silica microspheres are chemically treated such that neighboring CNCL molecules are forced to anchor normal to the sphere's surface [15]. When fully submerged in the CNCL, the anchoring conditions produce either a sequence of 180° point defects that wrap around the sphere to form a defect ring or a hedgehog point defect. These structures are displayed in Figure 3.9 and were known to exist prior to Tkalec et al.'s work.

Using laser tweezers, Tkalec et al. reversibly linked and manipulated the defect rings surrounding separate microspheres. By building an array of microspheres and then manually linking the individual defect rings, Tkalec et al. were able to assemble knotted defect structures of arbitrary complexity [16].

Another related technique that has successfully generated knotted structures uses colloidal rings and tubes rather than spherical particles. In the work of A. Martinez et al., the surfaces of colloidal tubes are treated using photopolymerization to encourage surface anchoring [17]. After treatment, the colloidal

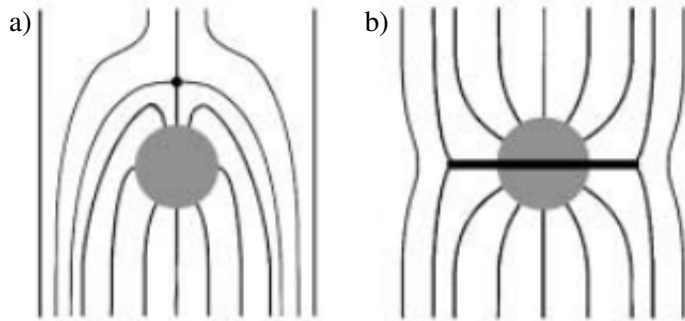


Figure 3.9: aligned phase of CNCL frustrated by a submerged silica microsphere that was chemically treated such that the CNCL anchors normal to the sphere. These boundary conditions can produce a a) hedgehog point defect or b) a wedge disclination loop (images from [15])

tubes are assembled into linked structures and then suspended in a non-chiral nematic liquid crystal. Anchoring to this colloidal template produces a linked pattern in the director field of the nematic [17].

While the above techniques produce defect structures that are a robust demonstration of the mathematics of knots at the micrometer scale, practical applications have not yet been identified. Applications to photonic devices, microscale assembly, or microfluidics are restricted by the rigid colloidal superstructure. This scaffolding diminishes the knot's potential utility by optically and physically blocking the interior of the knot and prohibiting dynamic manipulation. In this research, we pursued alternate means of defect induction that are not subject to those limitations.

3.4 Defect Induction via Boundary Conditions

In the simulations we conducted, defect structures were induced by fixing the orientations of the molecules on the boundary of the lattice. Alignment forces propagate this orientational information from the boundary into the interior. Experimentally, these boundary conditions could be enforced by chemically treating the liquid crystal container, atomic force microscopy etching, or through photopolymerization techniques [16, 17]. Depending on the specifics of the nematic liquid crystal, electric or magnetic fields could also orient the molecules on the boundary layer [3]. In our research, the structures investigated are comprised of a combination of wedge disclination loops (WDL) and pairs of disclination lines. In his thesis, Winoker attempted to thread these disclination lines through disclination loops [18]. Here we propose and demonstrate the boundary conditions that successfully produce this desired structure. We detail the methods used to widen and deform the disclination loops as well as techniques of blending disclination line and WDL boundaries.

3.4.1 Wedge Disclination Loops

As discussed in Section 3.1, disclination lines either run from boundary to boundary or form closed curves. These closed defect curves are often referred to as disclination loops. The 180° point defects that form the loops are either of the wedge or twist type. In a twist disclination loop, the rotation axis about which the molecules experience a 180° rotation is normal to the plane containing the disclination loop. In a wedge disclination loop, the rotation axis is tangent to the plane of the disclination loop. A single wedge 180° point defect is shown in Figure 3.10. Rotating the pattern about the dashed black line produces a wedge disclination loop.

In the lattice model, we can induce wedge disclination loops using radial boundary conditions: molecules on the boundary of the lattice have their orientational axis fixed to point toward the center of the lattice [19]. In Figure 3.11, these boundary conditions are displayed on four faces of a cubic 20 X 20 X 20 lattice. The expected location of the point defects can be approximately predicted by the following heuristic: construct a vertical line that connects the vertically oriented molecules at the top and bottom of the lattice and a horizontal line that connects the horizontally oriented molecules on the left and right faces of the lattice. The intersection of the vertical and horizontal lines gives the approximate location of the defect core.

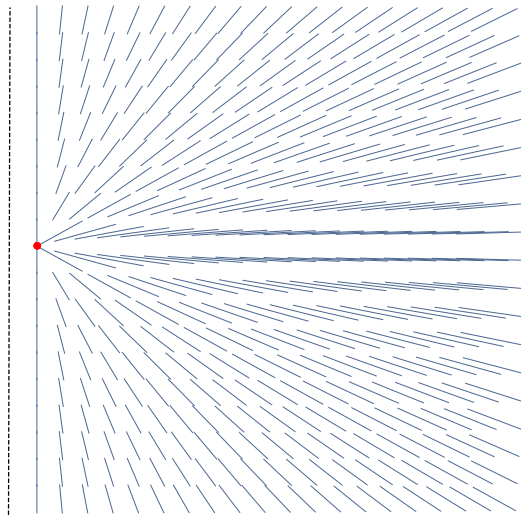


Figure 3.10: A two-dimensional slice of an idealized wedge 180° point defect induced via radial boundary conditions. The red dot marks the core of the defect. Rotating the pattern about the dashed line produces the wedge disclination loop structure.

Using this heuristic, we can control the width of the loop and the depth that it occurs in the lattice. Widening the loop requires moving the vertical orientation lines towards the edges of the bottom and top faces. The intersection with the horizontal orientation lines then produces defect cores away from the center of the lattice. To produce such cores, we deviate from the radial boundary conditions by vertically orienting the (otherwise radial) molecules in the centers of the top and bottom faces. To specify these boundary conditions, we introduce a vector field $\vec{O}(x, y, z)$ which describes the orientations of the molecules located at the point (x, y, z) . To produce a WDL with approximate radius R , radial boundary conditions are fixed on the left, right, front, and back faces of the lattice. The orientations on the top and bottom faces are given by

$$\vec{O}(x, y, z) = \begin{cases} \frac{(x, y, z)}{\sqrt{x^2+y^2+z^2}} & \text{if } x^2 + y^2 > R \\ (0, 0, 1) & \text{if } x^2 + y^2 \leq R \end{cases}$$

A sample WDL defect structure with $R = 40$ in a 100X100X10 lattice is presented in Figure 3.12. Given a larger lattice, this can be done in a smoother fashion by transitioning continuously between the vertical inner core and the radially oriented periphery. To do this, we introduce a blending (scalar) function $b(x, y)$ that is radially symmetric and is small near the origin and large far from it. For instance,

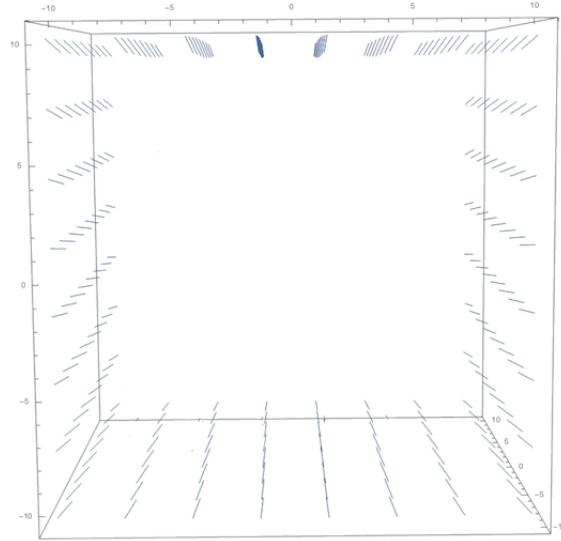


Figure 3.11: Radial boundary conditions on 20X20X20 lattice used for WDL defect induction. The front and back faces have been removed for ease of presentation.

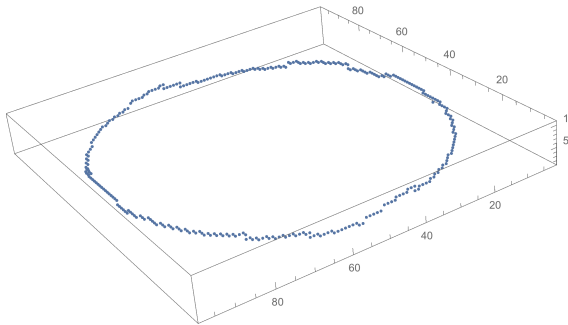


Figure 3.12: A wedge disclination loop in a 100X100X10 lattice with $R = 40$ set using the modified radial boundary conditions

$b(x, y) = e^{x^2+y^2/L}$ where L governs the width of the loop. The orientations on the top and bottom of the loop are then fixed according to

$$\vec{O}(x, y, z) = \frac{(e^{(x^2+y^2)/L}x, e^{(x^2+y^2)/L}y, z)}{\sqrt{e^{(x^2+y^2)/L}(x^2 + y^2) + z^2}}$$

3.4.2 Generalizing WDL Boundary Conditions

To produce other defect shapes, we can rely on the heuristic that defect cores form at the intersection of vertical and horizontal orientation lines computed from the boundary. For example, to produce an ellipse rather than a circular loop, molecules within the interior of the desired ellipse are oriented vertically and molecules exterior to the ellipse have radial orientations. This produces the ellipsoidal defect structure shown in Figure 3.13. Using this technique, we hypothesize that an arbitrary two-dimensional smooth closed curve can theoretically be constructed from defects in a sufficiently large lattice model. Radial

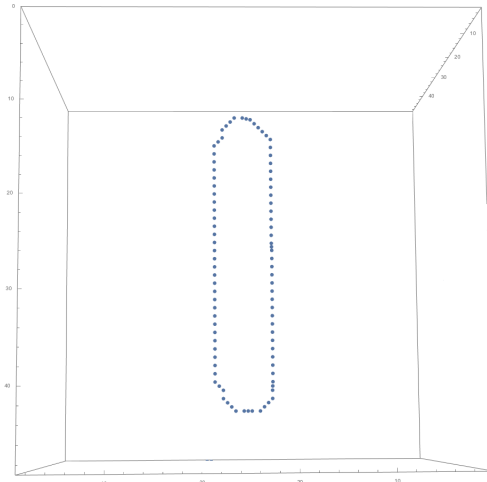


Figure 3.13: Ellipsoidal defect structure in a 50X50X50 lattice formed via the boundary conditions described in the text.

boundary conditions are set on four of the faces. We then project the desired curve onto the remaining two opposing faces. On each of these faces, molecules in the interior of the projection of the closed curve are aligned vertically. Molecules exterior to the curve are oriented radially. These boundary conditions produce the defect cores aligned in the shape of the desired curve roughly midway between the two opposing faces. The resolution of the resultant defect structure depends on the smoothness of the initial projection onto the opposing faces. For a given curve, increasing the number of lattice cells results in a smoother projection and greater fidelity between the resulting defect structure and the desired curve. For example, we illustrate this process for an arbitrary planar, closed curve such as $C(t) = (\cos(t) + \frac{1}{5} \cos(t), \sin(t) + \frac{1}{5} \sin(2t))$. The projection of this curve onto a face of the 60X60X60 lattice is shown (in black) in Figure 3.14. Note how discretization of the curve to the grid reduces the curve's smoothness and resolution. Molecules located at the red lattice points are in the curve's interior and have their orientations set to vertical. Molecules exterior to the curve at blue lattice points have their orientations point radially towards the center of the lattice. Two opposing faces of the lattice receive boundary conditions specified by Figure 3.14. The remaining four faces are given pure radial boundary conditions. After simulation, this produces the defect pattern in the interior of the lattice displayed in Figure 3.15.

These defect structures in the interior can be manipulated by dynamically adjusting the boundary conditions. We demonstrate this capability by first forming two independent wedge disclination loops in the interior as shown in Figure 3.16. On the boundary, the initially separate loop induction patterns are dynamically brought together to form an oval. As a result, the loop structures in the interior also converge and combine to form an oval. Then, the oval boundary conditions are transformed into the circular defect conditions which also morphs the interior defect structure from an oval to a circle. Using boundary conditions, we have thus combined two initially separate WDL's into a single loop. By reversing the procedure, the single loop can be re-separated into the initial two loops.

3.4.3 Threading Backer Lines Through Planar Curves

To create defect lines that course through the interior of the nematic cell and connect opposite faces of the lattice, we implement Backer boundary conditions [20]. Backer boundary conditions require that

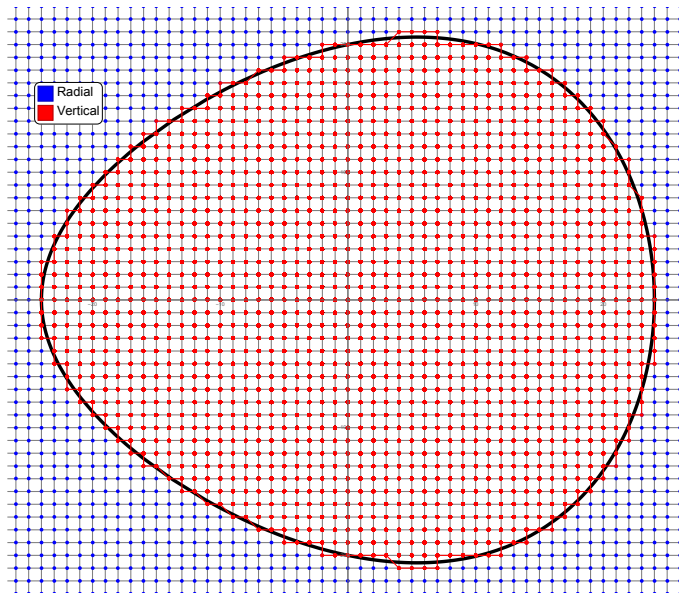


Figure 3.14: Boundary conditions on a face of the cubic lattice. $C(t) = (\cos(t) + \frac{1}{5} \cos(t), \sin(t) + \frac{1}{5} \sin(2t))$ is shown in black. This curve is discretized to a 60X60 grid. Molecules at red lattice points are vertically oriented and molecules at blue lattice points are radially oriented.

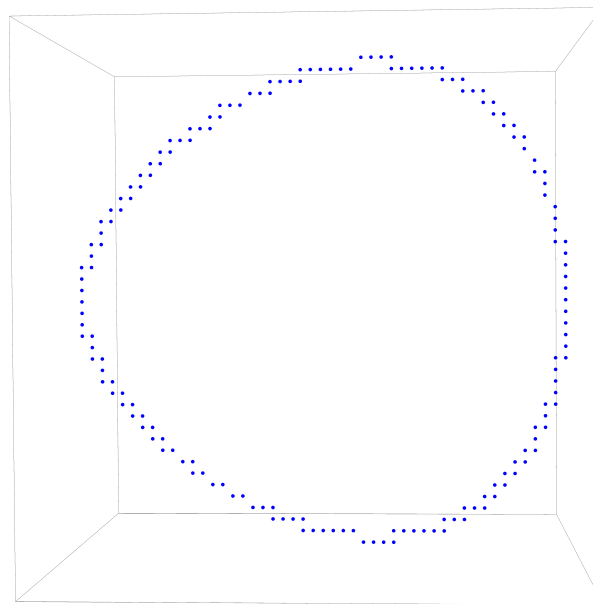


Figure 3.15: Defect structure produced by the boundary conditions described in the text and displayed in Figure 3.14

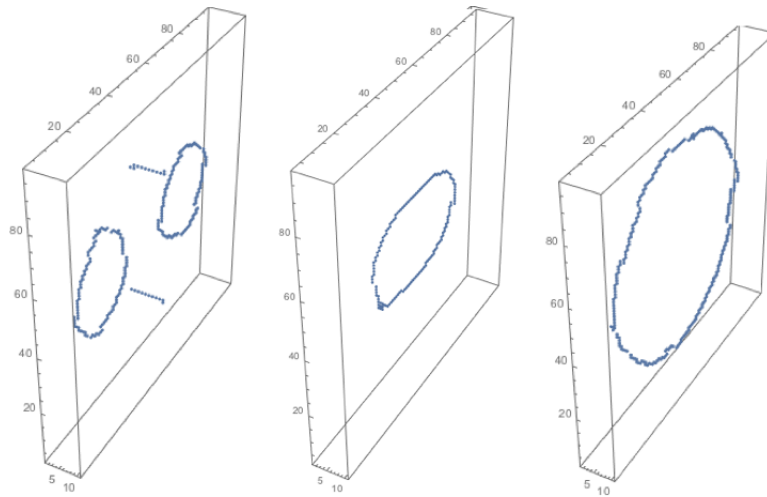


Figure 3.16: Snapshots of two separate WDL's evolving into a single defect loop using boundary condition manipulation

the molecules on two opposing faces of the lattice be oriented in a 360° point defect pattern as shown in Figure 3.17 [20]. Molecules on the other faces are subject to free or periodic boundary conditions [20]. The point defects frustrate the neighboring molecules and force a 180° disclination line to form and connect the defect cores on opposing sides of the lattice. In a sufficiently thick cell, the Frank free energy of the alignment pattern is minimized if two disclination lines course through the interior [20]. We will refer to this pair of lines as Backer lines. By creating an array pattern of these 360° point defects, an arbitrary number of Backer lines can be induced. In this research, we have focused on boundary conditions that produce a single pair of Backer lines as shown in Figure 3.18.

A natural question is whether Backer lines can coexist and thread through the planar closed curves described in the last section. Winoker attempted to achieve this via various techniques. These efforts relied on initially using pure radial boundary conditions to create a narrow wedge disclination loop [18]. After the loop stabilized, Winoker switched (in some cases abruptly and in others smoothly) to Backer boundary conditions [18]. This switch destroyed the initial loop and did not produce a stable, threaded structure [18]. Repeating those techniques on our model yielded identical results.

Using the methods developed in this chapter, we succeeded in producing the structure with a different approach. First, by using the planar curves algorithm, we built a very wide disclination loop that had an ample interior for Backer lines to penetrate. The process of switching from Backer boundaries at this stage was abandoned. Freed from the anchors on the boundary, the loop minimizes its energy by expanding until it is destroyed via collision with an edge of the lattice. We blend the WDL and Backer boundaries to form a composite set of boundary conditions that successfully punches Backer lines through the WDL.

Initial trials combined the WDL and Backer lines by discontinuously embedding 360° point defect within the vertical core of the WDL pattern. At the border of the point defect and the vertical core, the director experienced a 90° discontinuous rotation. Instead of coursing through the interior, defect lines connected the center of the Backer pattern to points on the boundary between the vertical layer and the Backer pattern. This problem was remediated by using non-cubic lattices with wide Backer patterns. For example, in Figure 3.19, a $100 \times 100 \times 10$ lattice is shown with a Backer pattern that extended to $R = 30$. These non-cubic geometries make it energetically favorable for the defect lines to cross to the opposite side of the lattice rather than the more distant Backer/vertical border.

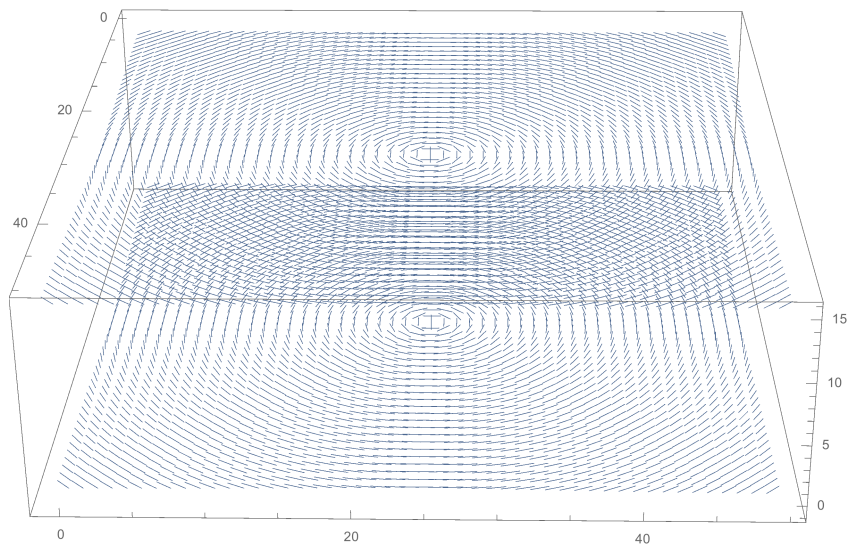


Figure 3.17: Backer boundary conditions: two opposing walls of the cell have 360° point defect patterns

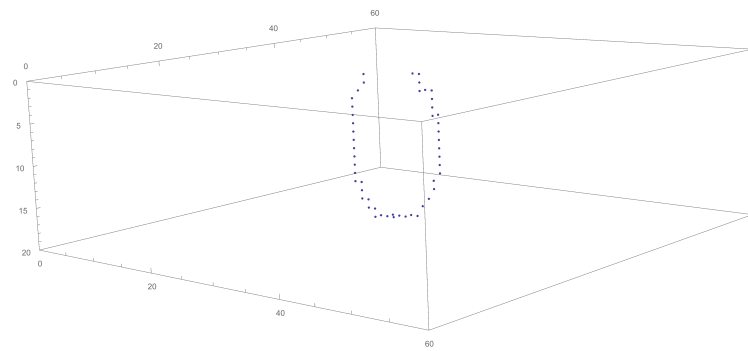


Figure 3.18: Backer lines coursing through a nematic cell with boundary conditions specified by Figure 3.17

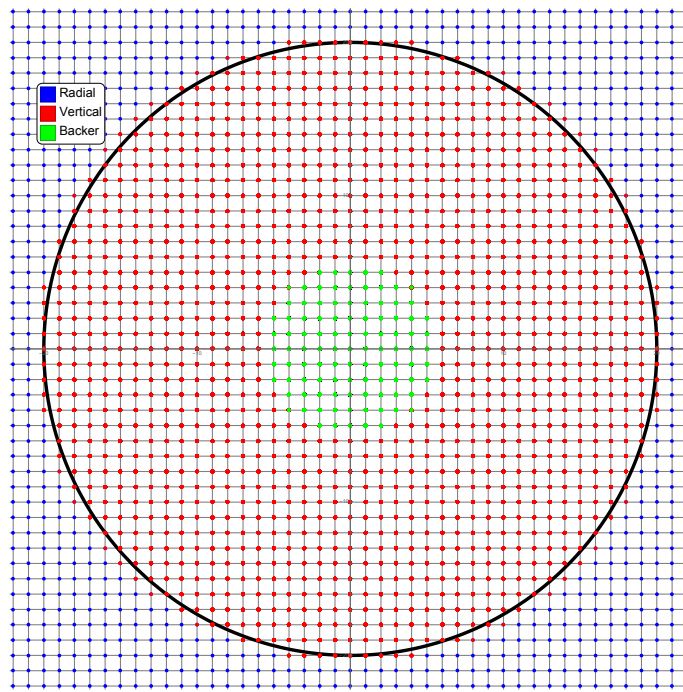


Figure 3.19: The composite boundary condition with a Backer pattern inserted in the center of the WDL's vertical core.

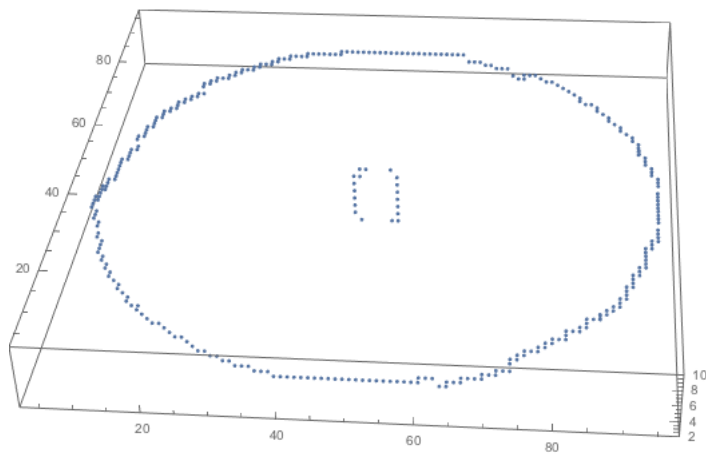


Figure 3.20: Backer lines threaded through a wide disclination loop.

Working in a more symmetrical lattice geometry, we produced a threaded structure by transitioning in a smoother manner between the vertical section and the horizontal Backer pattern. Given a lattice face with constant height, we introduced a vector field, $\vec{O}(x, y)$, which describes the orientations of the molecule. Let $\vec{V}(x, y)$ be the vector field specified by Backer boundary conditions and $\vec{W}(x, y)$ be the vector field that corresponds to disclination loop boundaries. To transition between them, we introduced $b(x, y)$, a blending function. Different functions were tried that were radially symmetric, small near the origin, and large far from it (e.g, $e^{x^2+y^2/L}$). Using the blending function, we specified the orientations according to

$$\vec{O}(x, y) = \frac{\vec{V}(x, y) + b(x, y)\vec{W}(x, y)}{|\vec{V}(x, y) + b(x, y)\vec{W}(x, y)|}$$

This smoothing process removed the sharp transition at the boundary between the vertical core of the WDL and the Backer pattern. The adjustment encouraged the Backer line to connect to the opposite face rather than twist back and terminate on the same face.

Both the blending technique and the non-cubic geometries successfully produced threaded structures as shown in Figure 3.20. Given a threaded structure, the disclination loop can be dynamically translated and widened by varying the WDL component of the boundary.. We hypothesize that the surrounding loop could also be deformed into any planar curve using a sufficiently high resolution lattice. Theoretically, a high resolution lattice would also allow multiple sets of Backer lines to penetrate through the wide disclination loop.

CHAPTER 4

Multispecies Models

In this chapter, we propose a generalization of the Lebwohl-Lasher model that allows for the simulation of mixed liquid crystals composed of multiple species of nematic molecules. The energy interaction prescribed by the model incorporates a rotationally-dependent term and a non-rotational cross-species interaction term. The model is designed to be capable of simulating a wide variety of mixing behavior, including species separation and variable cross-species alignment. In [21], a similar energy interaction was utilized to investigate nematic-isotropic phase coexistence in a binary mixture using grand canonical Monte Carlo simulations. In this research, however, the total number of molecules from each species is kept fixed throughout the simulation. To conduct Monte Carlo simulations of a multispecies model, exchange moves are introduced into the sampling procedure to account for changes in the positions of the molecules. We propose several schemes of incorporating exchange moves and contrast them using results from simulation. Finally, we close with a discussion of unresolved questions about the multispecies model and research directions suitable for future investigation.

4.1 Multispecies Lebwohl-Lasher Model

The research thus far concerned modeling liquid crystals that were composed of molecules all of the same species. In this chapter, we propose an extension of the Lebwohl-Lasher model designed to model the behavior of a liquid crystal composed of different species of nematic-like molecules. The nematic species could vary in length, molecular structure, polarity, etc. Inspiration for this modeling effort comes from experimental developments in the field of polymer-dispersed liquid crystals. In such materials, monomers are dispersed through a nematic liquid crystal. Exposure to UV light causes neighboring monomers to fuse and produce a hardened polymerized structure [22]. The interaction between the polymerized structure and the nematic liquid crystal results in novel electrical and optical properties [22].

In this research, we restrict our attention to multispecies models in which the alignment forces between neighboring molecules depend on their relative orientations and are well approximated by a Maier-Saupe-type energy interaction. By this we mean that the energy interaction between the i -th and the j -th neighboring molecules is proportional to $P_2(\cos(\theta_{ij}))$ where θ_{ij} is the angle between the long axes of the neighboring molecules. For the single species model, the constant of proportionality did not depend on the molecule in question and was fixed. For the multiple species model, the constant of proportionality varies depending on the species of the two molecules in question.

4.2 Multispecies Generalization of the Lebwohl-Lasher Model

As established in Chapter 2, we model a single species of nematic liquid crystals using the Lebwohl-Lasher model, in which the energy of the lattice is given by

$$E = -\epsilon \sum_{\langle ij \rangle} P_2(\cos \theta_{ij}) \quad (4.1)$$

where the sum runs over all neighboring molecules. To incorporate more than one species, we first let s_i be the species number for the i -th vector, where for a binary mixture $s_i = 1, 2$. To account for the species-dependent rotational interaction energy, we introduce a symmetric matrix ϵ , where ϵ_{lm} gives the characteristic energy for rotational interactions between the species l and m . The energy of the binary mixture is then given by

$$E = -\sum_{\langle ij \rangle} \epsilon_{s_i s_j} P_2(\cos \theta_{ij}) \quad (4.2)$$

where once again the sum runs over all neighboring molecules and θ_{ij} is the angle between the long axes of the i -th and j -th molecules. The sign of ϵ_{lm} governs the attractive or repulsive nature of the interaction and along with the temperature determines the macroscopic behavior of the model. In the standard Lebwohl-Lasher model, the Monte Carlo algorithm relies on single site rotation moves to sample the configuration space. In the more general multispecies model, we have to include moves that change the locations of the molecules in the lattice so that the entire configuration space is sampled. To this end, we will introduce moves that exchange the molecules at different lattice sites.

This model reduces to two non-interacting Lebwohl-Lasher models if $\epsilon_{ij} \propto \delta_{ij}$. The off-diagonal elements determine the cross-species interactions. In the case of

$$\epsilon = \epsilon \begin{pmatrix} 1 & 1 \\ 1 & 1 \end{pmatrix} \quad (4.3)$$

where the scalar ϵ has units of energy, all the interactions are identical and the model reduces to a single species Lebwohl-Lasher model. To illustrate the behavior of a less symmetrical case, suppose that

$$\epsilon = \epsilon \begin{pmatrix} 1 & -1 \\ -1 & 1 \end{pmatrix} \quad (4.4)$$

Since the off-diagonal terms are negative, the cross-species interaction favors misalignment and repulsion. In the low temperature limit, we expect that the species will separate into a configuration that minimizes the energy of the cross-species interface. Additionally, we expect that the directors of the individual species-separated regions should be orthogonal.

To account for species-dependent energy interactions that are rotationally independent, we introduce the fixed energy matrix, which we notate as \mathbf{f} . Incorporating this into the total energy results in

$$E = \sum_{\langle ij \rangle} (-\epsilon_{s_i s_j} P_2(\cos \theta_{ij}) + f_{s_i s_j}) \quad (4.5)$$

We have simulated models with this energy interaction for several different choices of $\epsilon_{s_i s_j}$ and $f_{s_i s_j}$. Future work is needed to completely categorize the model's behavior given the broad landscape of possible energy interactions.

4.3 Exchange Moves

In order to sample the entire configuration space of a binary mixture, we incorporated random exchange moves into the sampling procedure. As described in Algorithm 2, we first explored the effect of local exchange moves in which only neighboring molecules were selected for exchange. To understand the behavior of this sampling, we reduced the model to a two-dimensional lattice. First, simulations were run with no rotational interaction ($\epsilon_{ij} = 0$) and a fixed energy matrix given by

$$\mathbf{f} = \alpha \begin{pmatrix} -1 & 1 \\ 1 & -1 \end{pmatrix} \quad (4.6)$$

where α is a constant with units of energy. Because $f_{12} = f_{21} > 0$ and $f_{11} = f_{22} < 0$, this energy parametrization encourages species to separate into different domains. We conducted simulations over a range of temperatures. Models at high temperatures ($T > 5 \alpha/k_B$) produced equilibrium states that visually appeared very well mixed. At low temperatures ($T < .1 \alpha/k_B$), the simulation converged very slowly and the accepted move ratio declined quickly as the simulation progressed. The low acceptance ratio prompted concern about frozen-in states.

In order to rectify this issue, the exchange move procedure was reconsidered. Instead of local neighbor exchanges, the algorithm was modified such that global exchanges occurred between arbitrarily distant molecules on the lattice. This modification resolved the acceptance ratio concerns and we found the expected relationship between species-mixing and temperature. Several illustrative simulations are shown below:

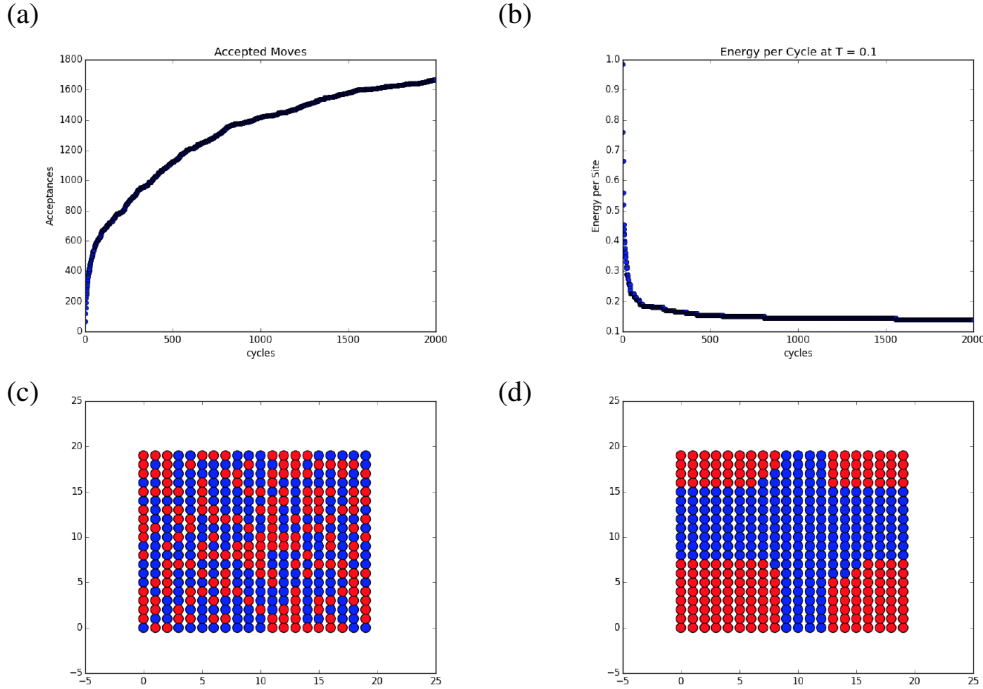


Figure 4.1: Results from a 2000 cycle simulation of a binary mixture with a low temperature of $T = .1 \alpha/k_B$ and periodic boundary conditions. The energy parametrization was specified by Equation 4.7 and sampling was conducted with global exchange moves. a) accepted moves versus exchange cycles b) stabilization of the energy per site c) randomly mixed initial conditions d) the final species-separated state after equilibration was reached

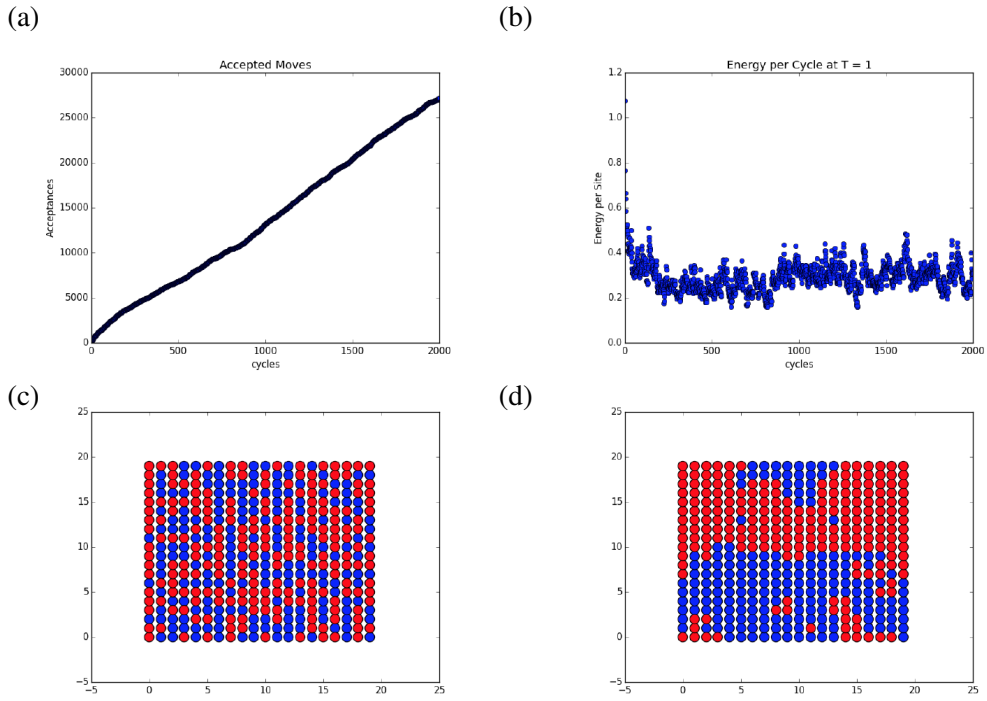


Figure 4.2: Results from a 2000 cycle simulation of a binary mixture with a moderate temperature of $T = 10 \alpha/k_b$ and periodic boundary conditions. The energy parametrization was specified by Equation 4.7 and sampling was conducted with global exchange moves. a) accepted moves versus exchange cycles b) stabilization of the energy per site c) randomly mixed initial conditions d) the moderately species-separated state after equilibration was reached

In Figure 4.1, we observe the expected low-temperature separation of the species. Note that from the plots of the accepted moves it is clear that global exchanges do not experience the critical slowdown encountered with local exchanges. To better understand global exchange moves, we also tried an alternative energy parametrization. In particular, we lowered the magnitude of the cross-species repulsion such that

$$f = \alpha \begin{pmatrix} 1 & -0.1 \\ -0.1 & 1 \end{pmatrix} \quad (4.7)$$

where α is a constant with units of energy. As expected, lower temperatures than the prior model were necessary to observe distinct species separation. To further validate the consistency of the model and sampling method, we also ran simulations with $f_{ij} = 1$. Results from those simulations revealed that there was no visual relationship between the degree of interspecies mixing and temperature.

4.4 Interspecies Mixing Correlation Functions

To rigorously characterize the degree of intermixing between the species, we propose a correlation function, $\phi_{ij}(d)$ that gives the relative number of molecules with species number i separated by a taxicab distance of d from molecules with species number j . The taxicab distance between the points \vec{p} and \vec{q} is given by

$$d(\vec{p}, \vec{q}) = \sum_{i=1}^3 |p_i - q_i| \quad (4.8)$$

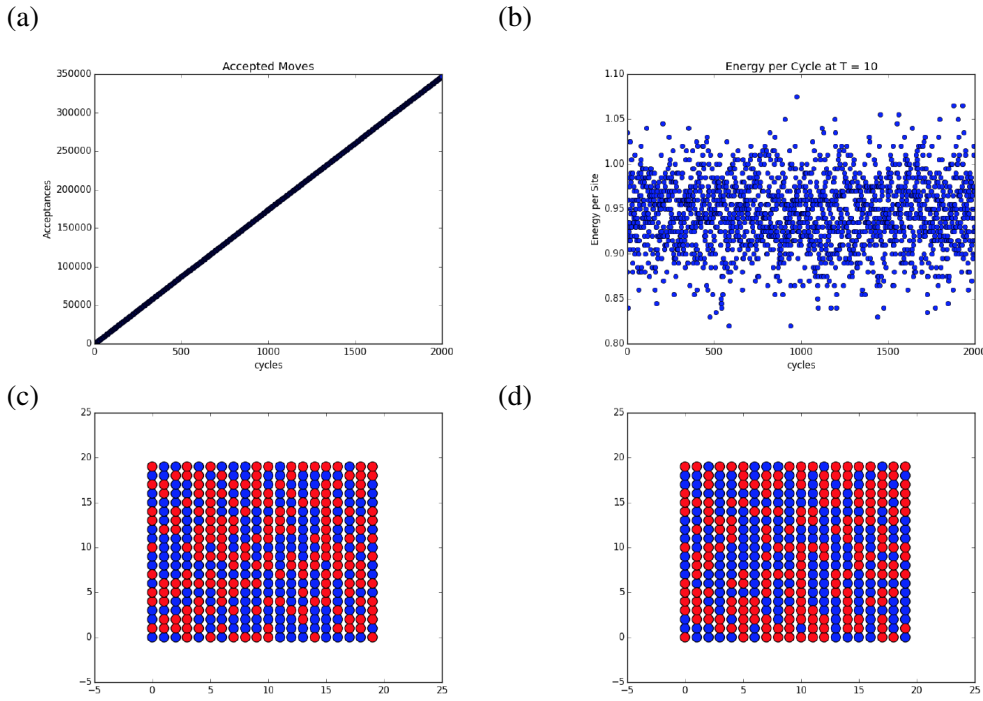


Figure 4.3: Results from a 2000 cycle simulation of a binary mixture with a high temperature $T = 10 \alpha/k_b$ and periodic boundary conditions. The energy parametrization was specified by Equation 4.7 and sampling was conducted with global exchange moves. a) accepted moves versus exchange cycles b) stabilization of the energy per site c) randomly mixed initial conditions d) the final well mixed state after equilibration was reached

The correlation function, $\phi_{ij}(d)$, can be computed using the following algorithm. Let D be the set of all lattice points and $s(p)$ give the species of the molecule at the lattice point $p \in D$.

Algorithm 3 Correlation Function Computation

- 1: Select a base lattice point $p \in D$
 - 2: Select a target lattice point $q \in \{D - p\}$
 - 3: Compute the taxicab distance $d(\vec{p}, \vec{q})$
 - 4: $\phi_{s(p)s(q)}(d(p, q)) = \phi_{s(p)s(q)}(d(p, q)) + 1$
 - 5: Repeat step 2 for all $q \in \{D - p\}$
 - 6: Repeat step 1 for all $p \in \{D\}$
 - 7: Independently normalize $\phi_{11}(d), \phi_{12}(d)$, and $\phi_{22}(d)$.
-

In Figure 4.4, we demonstrate how the correlation function reveals information about the distribution of the species in a $20 \times 20 \times 20$ lattice. For notational convenience, let $s = 1$ molecules be labeled as type A and let $s = 2$ molecules be labeled as type B. Figure 4.4a) shows the A-A correlation function for a lattice filled randomly with both species. For comparison, Figure 4.4b) shows the correlation function found for a model in which two $3 \times 3 \times 3$ diametrically opposite corners of lattice are filled with type A molecules and the remaining lattice points are filled with type B. The two peaks indicate the two distant clusters of type A molecules. The distribution of Figure 4.4c) results from filling the lattice in a configuration that resembles an ice-cream sandwich with the outer thirds (wafer) filled with type A and the center third (ice cream) with type B.

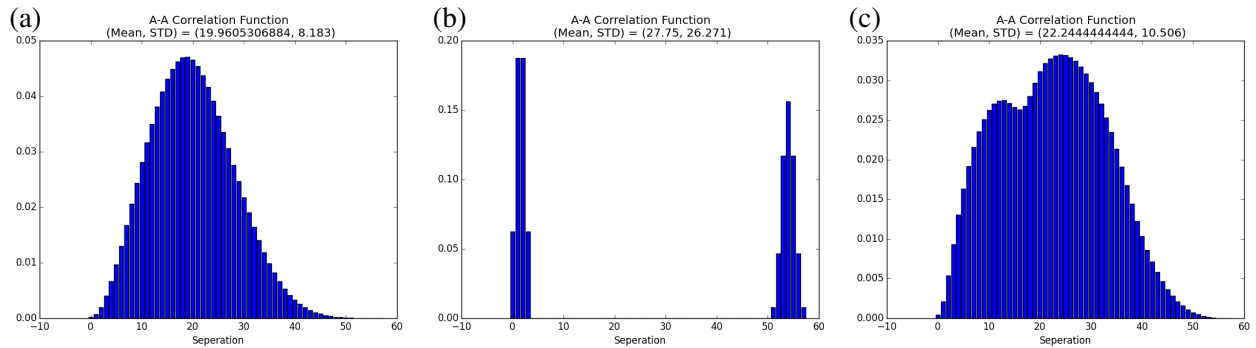


Figure 4.4: A-A correlation function distributions ($\phi_{11}(d)$) for a 20X20X20 lattice with the filling configurations specified in the text

4.5 Preliminary Results

For a model with a non-zero $\epsilon_{s_i s_j}$ term, the Monte Carlo algorithm sampling must incorporate both rotation and exchange moves. In doing so, care must be taken to satisfy the detailed balance condition and allow for the sampling to cover the entire accessible configuration space. The first implementation of a sampling procedure executed a lattice-wide exchange move cycle followed by a lattice-wide cycle of rotation moves. Test trials were conducted with the fixed energy matrix given by Equation 4.7 and a rotational energy matrix specified by Equation 4.3 with $\alpha = \epsilon$. This energy parametrization favors rotational alignment between all the molecules, but separation between the species. Time series of the energy per site showed large variations due to the exchange cycles. Even for long trials of 10,000 cycles, the energy time series did not visually show signs of convergence.

To encourage convergence, we altered the sampling procedure to make the changes in energy due to exchange moves more gradual. Instead of alternating between rotation and exchange lattice-wide cycles, we varied the move type from site to site. Procedures were tested in which the move type alternated or was randomly assigned. The implementation that produced the smoothest convergence randomly selected a rotation move or an exchange move followed by a rotation at the exchange sites. To better understand the behavior of this sampling scheme, we first reduced the lattice to be two dimensional. For simplicity, we also set the fixed energy matrix equal to zero. Therefore, the only difference between this model and the standard Lebowohl-Lasher model is the inclusion of the exchange moves. Trials were conducted on a 40 X 40 lattice with isotropic initial conditions.

As demonstrated in Figure 4.5, incorporating exchange moves lowered the energy of the system. In accordance with the lower energy result, the data displayed in Figure 4.6 reveals that exchange moves brought about more order. This behavior was observed at multiple temperatures and on a larger lattice of size 80 X 80. One possible explanation of this observation could have to do with the non-local nature of the exchange moves. Exchanging molecules while preserving their orientations allows for greater orientational communication across the lattice. On the other hand, we would expect the equilibrium distribution to be independent of the sampling procedure as long as the algorithm satisfies the detailed balance condition and samples from the full configuration space. To understand the significance of the observed differences in behavior between the sampling procedures, more runs and analysis are required.

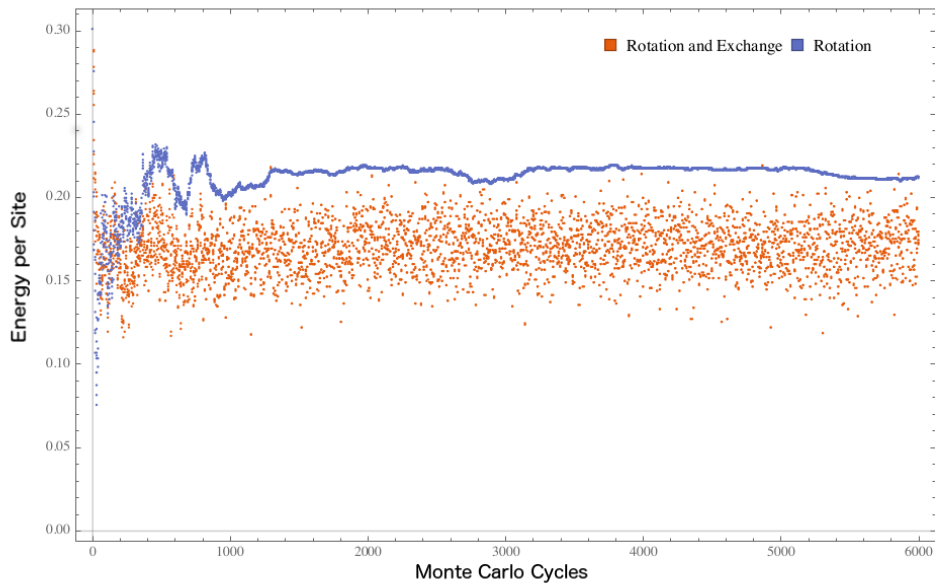


Figure 4.5: the energy per site results for $T = 5 \epsilon/k_b$ runs on a 40X40 lattice with sampling procedures of rotation only and with the inclusion of exchange moves

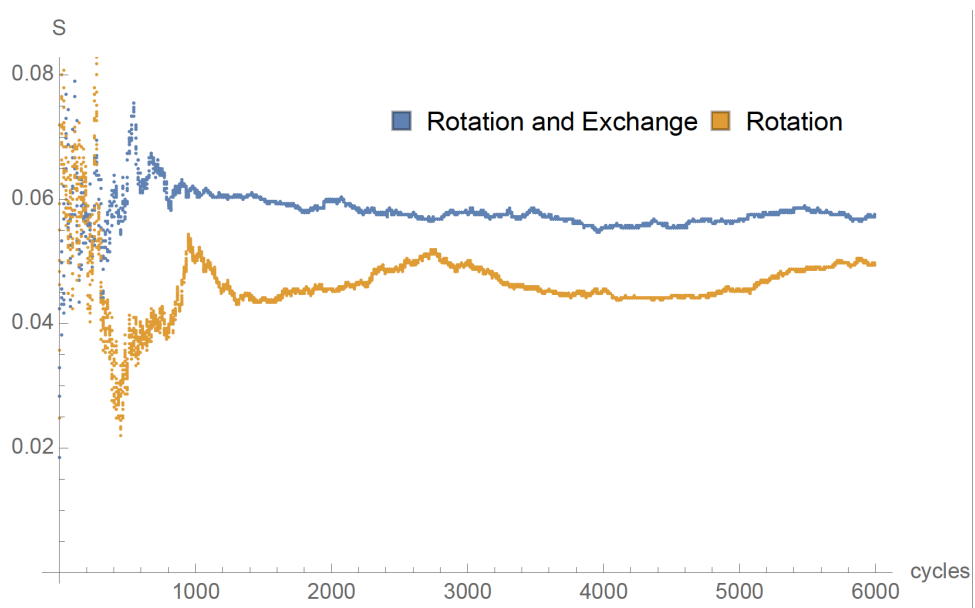


Figure 4.6: the scalar order parameter results for $T = 5 \epsilon/k_b$ runs on a 40X40 lattice with sampling procedures of rotation only and with the inclusion of exchange moves

4.6 Future Investigations

As mentioned in the prior section, achieving a more complete understanding of the behavior of models that incorporate exchange and rotation moves necessitates further investigation. In particular, the relationship between the length of the Monte Carlo run and the variability in the equilibrium energy and order parameter must be explored. Very long simulations with multiple seeds for each temperature should produce the data necessary to address how the combination of exchange and rotation moves alters the model's energy and order. Equipped with a better understanding of exchange moves, the rich landscape of the mixing behavior could be explored by running simulations with a variety of choices of the rotational and fixed energy matrices. It seems plausible that implementations of the model could produce equilibrium states of interest with novel degrees of species separation and interspecies alignment.

Bibliography

- [1] P. Chaikin and T. Lubensky, *Principles of condensed matter physics*, Cambridge University Press, 1995.
- [2] P. Collings, *Liquid Crystals: Nature's Delicate Phase of Matter*, 2nd ed., Princeton University Press, 2002.
- [3] M. Doi, *Soft Matter Physics*, Oxford University Press, 2013.
- [4] F. Vollrath and D. Knight, *Liquid crystalline spinning of spider silk*, Nature **410** (March 2001).
- [5] S. Hess, *Tensors for Physics*, Springer, 2015.
- [6] P. Lebwohl and G. Lasher, *Nematic-Liquid-Crystal Order–A Monte Carlo Calculation*, Physical Review A **6.1** (1972).
- [7] M. Allen and D. Tildesly, *Computer Simulation of Liquids*, 2nd ed., Oxford Science Publications, 1989.
- [8] R. Pathria and P. D. Beale, *Statistical Mechanics*, 3rd ed., Academic Press, 2011.
- [9] N. Metropolis et al., *Equations of State Calculations by Fast Computing Machines*, Journal of Chemical Physics **21** (1953).
- [10] N. Mermin, *The topological theory of defects in ordered media*, Reviews of Modern Physics **51.3** (1979).
- [11] I. Herstein, *Topics in Algebra*, 2nd ed., John Wiley and Sons, 1975.
- [12] V. Poenaru, *Elementary algebraic topology related to the theory of defects and textures*, Ill-Condensed Matter, Les Houches 1978 Lectures (1979).
- [13] M. Zapotocky and P. Goldbart, *Topological defects and the short-distance behavior of the structure factor in nematic liquid crystals* (1998), arXiv: [9812235 \[cond-mat\]](#).
- [14] M. Zapotocky, P. Goldbart and N. Goldfeld, *Kinetic of Phase Ordering in Uniaxial and Biaxial Nematic Films*, Reviews of Modern Physics **51.3** (February 1995).
- [15] U. Tkalec et al., *Reconfigurable Knots and Links in Chiral Nematic Colloids*, Science **333** (July 2011).
- [16] M. Ravnik et al., *Entangled Nematic Colloidal Dimers and Wires*, Physical Review Letters **99** (December 2007).
- [17] A. Martinez et al., *Mutually tangled colloidal knots and induced defect loops in nematic fields*, Nature Materials **13** (January 2014).
- [18] Z. Winoker, *Inducing Knotted Defect Structures in Nematic Liquid Crystals via Boundary Conditions*, Sc.B. Thesis, Brown University, 2013.

Bibliography

- [19] E. Terentjev,
Disclination Loops, Standing Alone and Around Solid Particles, in Nematic Liquid Crystals,
Physical Review E **51** (February 1995).
- [20] A. Backer, A. Callan-Jones and R. Pelcovits,
Nematic cells with defect-patterned alignment layers, Physical Review E **77** (2008).
- [21] J. Polson and E. Burnell,
Nematic-isotropic phase coexistence in a Lebwohl-Lasher model binary liquid crystal mixture,
Chemical Physical Letters **281** (December 1997).
- [22] D. Coates, *Polymer-dispersed Liquid Crystals*, Journal of Materials Chemistry **5** (2005).